frontiers | Frontiers in Ceramics

TYPE Review
PUBLISHED 08 January 2024
DOI 10.3389/fceic.2023.1307437

OPEN ACCESS

EDITED BY
Catalin Croitoru,
Transilvania University of Brașov,
Romania

REVIEWED BY
Ali Talimian,
Alexander Dubcek University in Trencin,
Slovakia
Ken Lee,
National Aeronautics and Space
Administration (NASA), United States

*CORRESPONDENCE
Ping Xiao,
p.xiao@manchester.ac.uk

RECEIVED 04 October 2023
ACCEPTED 29 November 2023
PUBLISHED 08 January 2024

CITATION
Scotson D, Paksoy AH and Xiao P (2024), Characterisation techniques for investigating TBC and EBC failure: a review.
Front. Ceram. 1:1307437.
doi: 10.3389/fceic.2023.1307437

Characterisation techniques for investigating TBC and EBC failure: a review

Daniel Scotson, Ahmet Hilmi Paksoy and Ping Xiao*

University of Manchester, Department of Materials, Henry Royce Institute, Manchester, United Kingdom

Materials characterisation plays a crucial role in developing thermal barrier coatings and environmental barrier coatings for gas-turbine engines. The failure of thermal barrier coatings and environmental barrier coatings is influenced by a complex interdependence of microstructure, residual stress, and thermomechanical properties. Validating our mechanistic understanding of each of these factors that contribute to failure requires a selection of suitable characterisation techniques. Presented in this review are characterisation techniques, both *ex situ* and *in situ*, that have advanced the understanding of thermal barrier coating and environmental barrier coating failure. Targeted coating development that is both effective and efficient depends on these characterisation techniques to obtain superior coatings with improved performance and lifetime.

KEYWORDS

characterisation techniques, environmental barrier coating, EBC, thermal barrier coating, TBC, failure

1 Introduction

Thermal barrier coatings (TBCs) and environmental barrier coatings (EBCs) facilitate using nickel based superalloys and silicon carbide composites respectively in demanding environments, such as the gas-turbine engine. Subjecting materials in a gas-turbine engine to ever more demanding environments is desirable to improve efficiency, accessed by increasing engine core temperatures. As a result, this reduces fuel burn, which simultaneously lowers operating costs and reduces environmental impact. However, limitations in the high-temperature performance (>1,200°C) and steam corrosion of the substrate materials require the introduction of TBCs and EBCs for protection.

The lifetime of TBCs and EBCs is dependent on their many failure mechanisms arising because of their demanding, operating environment. This environment typically involves thermal cycling, steam exposure and ingested contaminants, such as calcium magnesium alumino-silicates (CMAS), that can also result in solid particle erosion and foreign object damage (FOD) (Spitsberg and Steibel, 2004; Lee, 2018; Padture, 2019). Commonly, these conditions occur simultaneously, posing challenges to accurately model and predict the evolution of coating properties throughout lifetime.

Understanding TBC and EBC failure and consequently developing coatings with longer lifetimes is therefore only possible with an extensive use of characterisation techniques. Characterisation techniques, both *ex situ* and *in situ*, evidence the evolution of microstructure, residual stresses and thermomechanical properties throughout lifetime, Figure 1. This leads to a better understanding of the complex interplay between these factors contributing to coating failure. Understanding their failure then facilitates the targeted development of more effective coatings by tailoring compositions and obtaining better microstructures to extend lifetime.

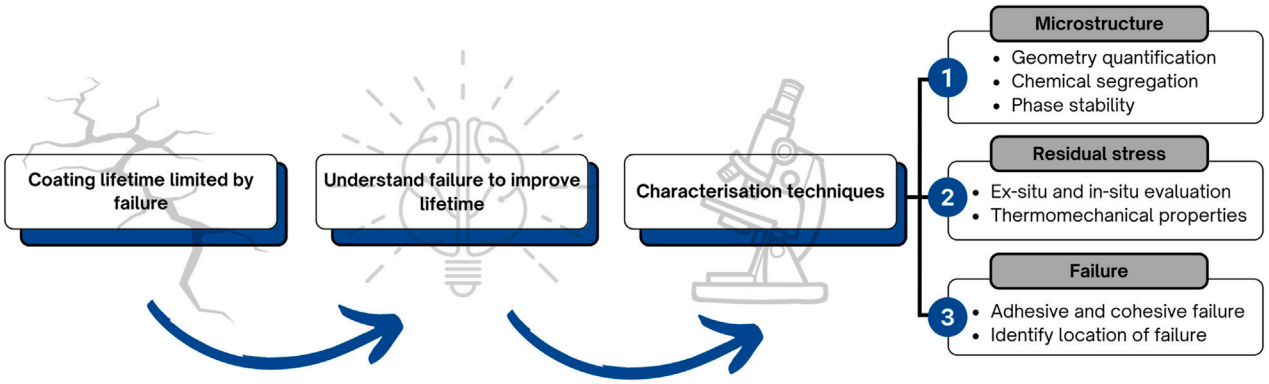

FIGURE 1
Outlining the role of characterisation techniques to understand the failure of thermal barrier coatings (TBCs) and environmental barrier coatings (EBCs).

2 Purpose of TBCs and EBCs

TBCs are designed to thermally insulate nickel based superalloy components from the gas-turbine engine core's operating temperature. Typical TBC systems consist of two layers: a ceramic top coat (6-8 wt% Y_2O_3-ZrO_2) and a metallic bond coat (NiCoCrAlY, β-(Ni,Pt)Al or Pt-diffused γ/γ'-based NiAl). Commonly resulting in a millimetre scale TBC, the coating must then have a low thermal conductivity to insulate the nickel based superalloy from a combustion environment that is now hotter than the superalloy's melting temperature. Publications highlighting the development of TBC systems can be found elsewhere (Miller, 1997; Evans et al., 2008; Clarke et al., 2012; Ghosh, 2015; Bakan and Vaßen, 2017; Gopal Thakare et al., 2021).

A step change to engine performance requires even higher engine core temperatures, which means replacing nickel based superalloys with silicon carbide (SiC) based composites. SiC composites' advantages include: higher temperature capability (above 1,200°C); higher creep resistance, and lower density (1/3rd of nickel based superalloys) (Lee, 2000; Spitsberg and Steibel, 2004). Consequently, the introduction of SiC composite components results in weight reduction and removes the need for additional cooling infrastructure, which increases the available air for combustion to generate engine thrust (Lee et al., 2021). Therefore, next-generation gas turbine engines can achieve currently unattainable thrust to weight ratios (Lee et al., 2021).

Despite these advantages, SiC in the combustion environment of a gas-turbine engine is susceptible to steam corrosion at an unacceptable rate of 1 μm/h at 1,200°C (Jacobson, 1993; Opila et al., 1999). Therefore, EBCs are required to protect SiC (Eaton et al., 2000; Eaton and Linsey, 2002; Kimmel et al., 2002) and enable even higher efficiencies in the gas-turbine engine (Spitsberg and Steibel, 2004).

A common EBC system, with a sub-millimetre thickness, is composed of a mixed rare-earth silicate (i.e $Yb_2Si_2O_7$/Yb_2SiO_5) top coat and a silicon bond coat. Advantages of these silicate based top coats include their stability at high-temperatures and their lack of polymorphs and resulting phase transformations. Their thermal expansion coefficient is also similar to SiC (4.5×10^{-6} °C^{-1} (Padture, 2019)), which prevented the established TBC system containing zirconia-based materials (10×10^{-6} °C^{-1} (Hayashi et al., 2005)) protecting SiC. The silicon bond coat improves the adhesion between the coating and substrate (Kane et al., 2021), but the silicon imposes a temperature limit to an EBC, given its melting temperature of ~1,416°C (Desai, 1986; Zhang et al., 2022). Therefore, this has started the development of alternative EBC systems with different bond coats (Anton et al., 2020; Harder, 2020; Lee et al., 2022; Zhang et al., 2022). Comprehensive reviews of other EBC systems and compositions can be found in separate publications (Tejero-Martin et al., 2021; Paksoy and Xiao, 2023).

3 Failure mechanisms of TBCs and EBCs

The extreme and complex in-service environmental conditions of TBCs and EBCs, which can simultaneously involve thermal cycling, steam oxidation and CMAS interaction, result in various failure mechanisms.

For TBCs, the thermally grown oxide (TGO), formed at temperatures exceeding 700°C at the bond coat/top coat interface (Stott and Wood, 1987; Takahashi et al., 2019), highlights the need for a holistic approach to understand its associated failure. The TBC TGO can contain a variety of phases dependent on the underlying bond coat; these include α-Al_2O_3 and mixed oxides, potentially consisting of metastable alumina, zirconia and $NiAl_2O_4$ spinel phase (Stiger et al., 1999; Chen et al., 2012). Consequently, residual stresses can then arise from TGO growth, and also from the thermal mismatch between the TGO and adjacent coating layers (Evans et al., 2001). These stresses can then result in buckling and spallation of the coating, initiated at imperfections in the TGO (Evans et al., 2001). Identifying the mechanisms that cause these residual stresses is important to understand their interplay with microstructural evolution.

Similarly, oxidation of EBCs forming a SiO_2 TGO is an important failure site. Silicon bond coat oxidation occurs with a typical parabolic growth rate at micrometre thicknesses (Deal and Grove, 1965; Jacobson, 1993; Richards et al., 2016) and residual stresses arise from the difference in bulk thermal expansion coefficients between coating layers. These include: silicon (4.1×10^{-6} °C^{-1} (Desai, 1986; Richards et al., 2016)), one of the most used EBC top coat materials, $Yb_2Si_2O_7$ (4×10^{-6} °C^{-1} (Fernandez-Carrion et al., 2013)), and an α-cristobalite, SiO_2 TGO (30×10^{-6} °C^{-1} (Peacor, 1973; Perrotta et al., 1989)). Consequently, multi-layer models estimate thermal mismatch stresses of 4 GPa in the TGO (Richards et al., 2016; Begley and Hutchinson, 2017). However, these models assume planar interfaces, and that there is no stress relief by cracking or creep deformation (Richards et al., 2015; Richards et al., 2016;

Begley and Hutchinson, 2017). An added complication for modelling is representing the complex, inhomogeneous microstructures achieved by thermal spray processes, such as air plasma spray (APS). Therefore, an evaluation of these coatings' thermomechanical properties and residual stresses is required to validate the suitability of these simplified models.

Furthermore, the EBCs' high temperature cubic, β-cristobalite SiO_2 TGO also transforms to the tetragonal α-cristobalite phase upon cooling at approximately 220°C (Evans et al., 2001; Richards et al., 2016). The associated 4.5% volume shrinkage upon cooling can initiate cracks to cause coating spallation (Evans et al., 2001; Breneman and Halloran, 2014; Richards et al., 2016). *In situ* characterisation techniques to evaluate the resulting microstructure changes and residual stresses as a function of temperature are consequently important here.

The morphology of the TBC TGO also affects failure. Repeated thermal cycling can result in a roughening of the TBC bond coat, termed ratcheting, which propagates top coat cracks on each thermal cycle, before eventual crack coalescence and coating spallation (Evans et al., 2001). Therefore, models assuming planar interfaces are unsuitable given the concave and convex interfacial regions more closely resemble a misfitting sphere model (Evans et al., 2001). Furthermore, these models need to incorporate the microstructural evolution to track the change in residual stress distribution along an undulating interface, and the residual stress relief provided by cracking. Consequently, tracking the evolution of microstructure, determining the thermomechanical properties, and evaluating the local distribution of residual stress are all required to fully understand the TGO's role in TBC failure.

As well as undulations at the TGO interface, an increased TGO thickness also increases the likelihood for failure. Considering an energy-based approach for fracture, a thicker TGO increases the strain energy release rate, increasing the driving force for crack propagation and coating delamination (Hutchinson and Suo, 1991; Evans and Hutchinson, 1995; Begley and Hutchinson, 2017). Therefore, a critical TGO thickness is a simple failure criterion, commonly cited for both TBCs (Evans et al., 2001) and EBCs (Richards et al., 2016).

Reducing and controlling the TGO growth rate are therefore approaches pursued for both TBCs and EBCs. These include altering the bond coat morphology with TBCs (Gil et al., 2006; Yanar et al., 2006; Martins et al., 2020) and for EBCs, making top coat additions, such as Al_2O_3 or Al_2O_3-containing compounds including mullite and YAG ($Y_3Al_5O_{12}$) (Lee, 2018; Lee et al., 2021; Paksoy et al., 2022) Validating these approaches requires quantifying the thermal oxide thickness by evaluating microstructure evolution throughout lifetime from deposition to failure.

However, since coating delamination is typically life-limiting, this involves mixed-mode loading propagating interfacial cracks between dissimilar materials (Piva and Viola, 1980; Liechti and Hanson, 1988; Hutchinson and Suo, 1991). Inducing this failure mode with representative loading boundary conditions is difficult. Hence, the evaluation of the fracture toughness is simplified to individual coating layers, meaning that nanoindentation or micromechanical approaches (Di Maio and Roberts, 2005) are necessary to satisfy the assumptions that the crack size is much smaller than the sample geometry (Irwin, 1948; Irwin, 1957; Lawn, 1993).

Another environmental challenge for TBCs and EBCs is the ingestion of siliceous contaminants into a gas-turbine engine. These can include sand, salt, and volcanic ash, also termed calcium magnesium alumino-silicates (CMAS) (Kim et al., 1993; Poerschke et al., 2017; Cao et al., 2021). The reaction of the coating and CMAS can cause dissolution-reprecipitation of new phases, and at very high temperatures (i.e. >1,100°C), the infiltration of molten CMAS through porosity and grain boundaries (Stott et al., 1994; Borom et al., 1996; Grant et al., 2007; Levi et al., 2012). The infiltration of CMAS can also lead to a loss of strain tolerance, provided by the columnar structure of TBC top coats deposited by electron-beam physical vapour deposition (EB-PVD) (Mercer et al., 2005; Evans and Hutchinson, 2007; Krämer et al., 2008). Understanding the mechanisms of infiltration, phase transformation and microstructural evolution inform the choice of coating compositions that are stable, and also microstructures that provide enhanced CMAS protection (Cao et al., 2021; Morelli et al., 2022).

Furthermore, the physical interaction of ingested contaminants can also result in solid particle erosion and foreign object damage (FOD) of coatings (Wellman and Nicholls, 2004; Bhatt et al., 2008; Gohardani, 2011; Presby et al., 2023). Erosion can also reduce the thermal insulation provided by the coating from a reduction in thickness and thus accelerate TGO growth for failure (Wellman and Nicholls, 2008). This highlights the need for testing in representative environments to establish the links between multiple environmental conditions, for example, between steam oxidation and foreign object damage (Hoffman et al., 2023) that together accelerate coating failure.

In conclusion, a wide variety of failure mechanisms occur in complex multi-layered TBC and EBC systems operating in extreme environments. All these failure mechanisms involve a complex interplay between microstructure, residual stresses, and thermomechanical properties. As a result, it is challenging to obtain reliable and representative models, meaning that characterisation techniques are essential to understand failure and then develop coatings with predictable performance throughout lifetime.

The following sections detail techniques suited to characterising microstructure (Section 4), evaluating stress (Section 5) and also inducing failure (Section 6) in TBCs and EBCs.

4 Characterising microstructure

4.1 Morphology evolution

Characterising a coating's morphology is necessary to study its evolution as a function of its extreme environmental conditions. There are several microstructural features of particular interest for TBCs and EBCs; these include the top coat grain size and grain orientation, and also the top coat's porosity. Additionally, the oxide layer thickness and bond coat roughness play a significant role in the interfacial failure mechanisms related to the TGO.

Furthermore, once failure mechanisms are established, the visualisation of the microstructure is an important feedback loop for optimising coating processing to avoid failure (Whitehouse, 1997). For example, achieving a grain size that reduces steam permeation (Wada et al., 2017; Kitaoka et al., 2018; Matsudaira et al., 2021); optimising the orientation of porosity for strain tolerance (Singh and Wolfe, 2005; Mauer and Vaßen, 2020), or obtaining a suitable interfacial roughness for adherence without increasing the likelihood for failure by ratcheting or rumpling (Evans and Hutchinson, 1984).

The following sections present the application of various characterisation techniques visualising and quantifying microstructural features in the top coat (4.1.1), thermally grown oxide (4.1.2) and bond coat (4.1.3) in TBCs and EBCs.

4.1.1 Top coat

Porosity in the top coats of TBCs and EBCs has both advantages and disadvantages. Porosity present between EB-PVD columns or between APS splats is essential for ensuring stress compliance during extreme thermal cycling conditions (Fleck et al., 2014). However, porous coatings can also increase the rates of CMAS corrosion by providing pathways for diffusion or infiltration (Naraparaju et al., 2017; Tejero-Martin et al., 2022). Furthermore, pores can accelerate the steam corrosion of the $Yb_2Si_2O_7$ EBC top coat (Mccormack et al., 2023), affect the resistance to foreign object damage (Wellman and Nicholls, 2007; Kedir et al., 2020), and increase solid particle erosion (Presby et al., 2023). Thus, porosity is a parameter influencing TBC and EBC performance, and evaluating its evolution is important to obtain predictable performance (Nakamura et al., 2000; Tejero-Martin et al., 2021).

There are many methods to evaluate porosity within coatings. The Archimedes method is simple (ASTM International, 2013), but cannot quantify a distribution of pore sizes as achieved with mercury intrusion porosimetry (MIP) (Siebert et al., 1999; Medricky et al., 2015). However, both these techniques cannot indicate the spatial distribution of pores. This is important as densification gradients, due to sintering, can lead to elastic modulus variation as a function of depth into a coating (Kulkarni et al., 2006; Fleck et al., 2014). Other techniques include X-ray computed tomography (XCT) to provide this spatial distribution, although its resolution is limited (>1 μm), while SEM offers improved resolution, but the investigated region is limited to the sectioned area.

Characterisation techniques with improved resolution are also required since EB-PVD TBCs contain nanometre scale porosity. Capable techniques include small angle neutron scattering (SANS) and transmission electron microscopy (TEM) (Kulkarni et al., 2006). For example, *in situ* SANS at temperatures up to 1,100°C and laser flash analysis indicate pore coarsening increases the thermal conductivity after thermal ageing (Saruhan et al., 2011). The development of anisotropic intra-columnar porosity, observed with bright field TEM images after isothermal ageing (over 100 h at 1,100°C), also explains the plateauing of thermal conductivity with thermal ageing of a fully-stabilised EB-PVD YSZ top coat (Saruhan et al., 2011). The limited sample volume of a TEM lamella, means that significant effort is required to reliably investigate any evolution of this porosity.

Measuring the grain size and determining the grain boundary density is another common and straightforward microstructural feature to quantify. As EBC top coat grain boundaries are pathways for both steam permeation (Wada et al., 2017; Kitaoka et al., 2018; Matsudaira et al., 2021) and CMAS infiltration (Sternlicht et al., 2022b), determining the grain size can provide a measure of the EBC's corrosion resistance. Additionally, measuring grain size can evaluate grain coarsening during thermal exposure (Yilmaz et al., 2023), or understand the effect of secondary phases pinning grain boundaries (Paksoy and Xiao, 2021). For this measurement of grain size, electron backscattered diffraction (EBSD) (Humphreys, 2001) or image processing of SEM micrographs are standard methods (ASTM International, 2021b). More traditional methods using intercept methods (Heyn, 1903; Abrams, 1971) are unsuitable given the heterogeneity with thermal spray microstructures.

Grain orientation can also affect thermal conductivity (Zhu and Miller, 2000) and CMAS infiltration (Naraparaju et al., 2017), especially with the highly orientated columnar structure of EB-PVD TBCs. Identifying the intensity variation of X-ray diffraction (XRD) pattern peaks and SEM cross-section micrographs can determine suitable preheating temperatures and deposition times to achieve well-orientated and strain tolerant EB-PVD TBC columnar structures (Czech et al., 1999; Wada et al., 2004).

4.1.2 Thermally grown oxide

Examining a coating's cross-section is a common characterisation approach for assessing the evolution of oxide layers. Microstructures can be imaged with SEM or optical microscopy, with the greyscale contrast variation aiding the identification of oxide layers, Figure 2 (Ridley et al., 2022; Ridley et al., 2023). Capturing high-resolution SEM micrographs of oxide layers with automated sample stages and then stitching these images enables the measurement of thickness variation across significant regions of interest (Ridley et al., 2022, Ridley et al., 2023). For example, cross-sectioning identified that the EBC top coat thickness is not a limiting factor in TGO thickness, suggesting that the diffusion of oxidants across the TGO is the growth rate limiting mechanism (Lee, 2018; Lee et al., 2021; Lee et al., 2021).

Methods for segmenting microstructural features, such as oxide layers, are also advancing. Software tools, such as AutoTracer (Su et al., 2021), CMAT (Su et al., 2021) and SOFIA (Stack, 2022), provide a user-interface to segment images and identify the oxide according to greyscale contrast. This automation streamlines the measurement of oxide thickness and roughness, Figure 2 (Ridley et al., 2022; Ridley et al., 2023). Additionally, automatic segmentation with machine learning driven approaches is progressing. For instance, the successful segmentation of EBC oxides has been achieved through transfer learning and MicroNet, a training dataset of over 100,000 microscopy images (Stuckner et al., 2022). Providing open access to these methods leads to greater standardisation and ultimately offers more reliable comparison of TGOs formed in different environments with a variety of coating microstructures and compositions.

4.1.3 Bond coat

Measuring the bond coat's roughness evolution with thermal cycling can be performed with confocal microscopy (Evans et al., 2001). Confocal microscopy reveals the 3D morphology of an exposed surface, such as an oxidised TBC bond coat (Chen et al., 2017; Martins et al., 2020). Correlating between roughness datasets from confocal microscopy and TBC lifetime, enabled the definition of a Total Thresholded Surface Area parameter (Martins et al., 2020). Notably, this parameter reflected the bond coat morphology and showed that bond coats with broad, symmetric peaks resulted in longer lifetimes than bond coats with steep, narrow, asymmetric peaks (Martins et al., 2020).

However, confocal microscopy cannot characterise bond coats or TGOs when a top coat is present. Therefore, for real coating systems, other non-destructive techniques are necessary. An alternative approach is XCT, which has tracked the TBC bond coat roughness evolving with thermal exposure time (Zhao et al., 2012). XCT has also provided insight into the 3D crack geometry relative to the bond coat's peaks and troughs, Figure 3 (Ahmadian et al., 2015). Moreover, XCT identified cracks initiated at off-peak

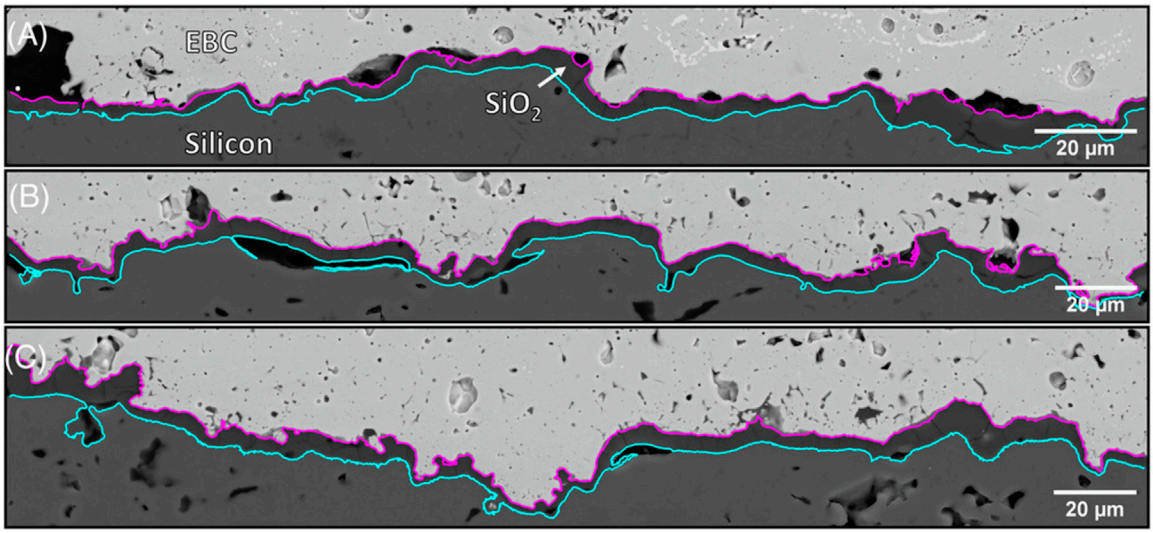

FIGURE 2
Evolution of an EBC SiO_2 TGO layer with steam cycling. **(A)** 120 **(B)** 300 and **(C)** 500 cycles with each cycle consisting of a 1-h exposure at 1,350°C with a 10-min air quench cool and calculated steam flow rate of 1.5 cm s^{-1}. Blue and pink lines indicate evaluated contours by image thresholding performed by SOFIA software (Stack, 2022). Reprinted from Ridley et al. (2022) with permission from Elsevier.

bond coat locations rather than on the peaks (Ahmadian et al., 2015), further highlighting the effect of bond coat morphology influencing failure.

4.1.4 Technique overview

Table 1 provides an overview of techniques for characterising the morphology of TBCs and EBCs.

The morphology features of particular interest include the top coat grain size and the TGO interface roughness on representative regions of interest to reliably inform of their evolution and spatial variation. SEM and EBSD, additionally with stitching, provide suitable regions of interest (centimetre-scale) at high resolution (tens of nanometres). However, these techniques are only representative of the prepared slice of material. Confocal microscopy is advantageous for quantifying interfacial roughness of exposed surfaces. Although, this limits any study of bond coat roughness evolution with confocal microscopy as a top coat cannot be present or must be removed.

Alternatively, XCT provides a 3D perspective of the entire coating, with a useful interpretation of porosity. However, the limited resolution (>1 μm) and restricted penetration depth without specialist synchrotron facilities limit XCT's application in characterising ceramic coatings. A representative quantification of porosity at high resolution, while also mapping its spatial distribution is a limiting factor for characterisation techniques with a safer alternative to MIP not currently available.

4.2 Assessing chemistry and phase analysis

The high-temperature environment of TBCs and EBCs means that oxidation, phase transformations and amorphous/crystalline transitions all occur. Affecting these processes are diffusion mechanisms, composition effects and elemental segregation. The characterisation techniques informing their roles in TBC and EBC failure are outlined in this section.

4.2.1 Top coat

With EBCs, crystalline, crack-free top coats are preferred to reduce TGO formation. Typically this involves performing a heat-treatment (above 1,200°C) to crystallise the amorphous phases present after APS deposition, given the high cooling rates (Richards et al., 2015; Garcia et al., 2019; Xiao et al., 2020). Choosing suitable heat-treatment temperatures is important as metastable phases can induce volumetric changes from phase transformations that also affect the porosity and micro-crack density (Garcia et al., 2021; Bakan and Vaßen, 2023).

In situ variable temperature XRD is valuable in identifying such an amorphous to crystalline phase transformation and tracking the EBC top coat's evolution at temperatures of interest, Figure 4 (Garcia et al., 2021). In an investigation of a $Yb_2Si_2O_7$-based EBC system, the top coat's amorphous to crystalline transformation started at around 1,050°C. Furthermore, the heat treatment temperature determined the crystallised phase; above 1,220°C resulting in the stable β-$Yb_2Si_2O_7$ phase, rather than metastable phases (Garcia et al., 2021). These metastable phases were also only present with particular processing conditions, Figure 4B, so *in situ* variable temperature XRD can inform the choice of desirable EBC processing parameters.

For TBCs, the yttria doped zirconia top coats can transform due to the limited composition variation of its phase fields (Scott, 1975). Furthermore, top coats are typically only partially stabilised with yttria to obtain better erosion resistance, which inherently means the phase stability needs understanding through operation (Stecura, 1978; Fang et al., 1999; Medvedovski, 2001; Reed, 2006). The yttria content and hence the ZrO_2 phase has a large effect on the thermal cycling lifetime (Stecura, 1985; Miller, 1987). For example, the

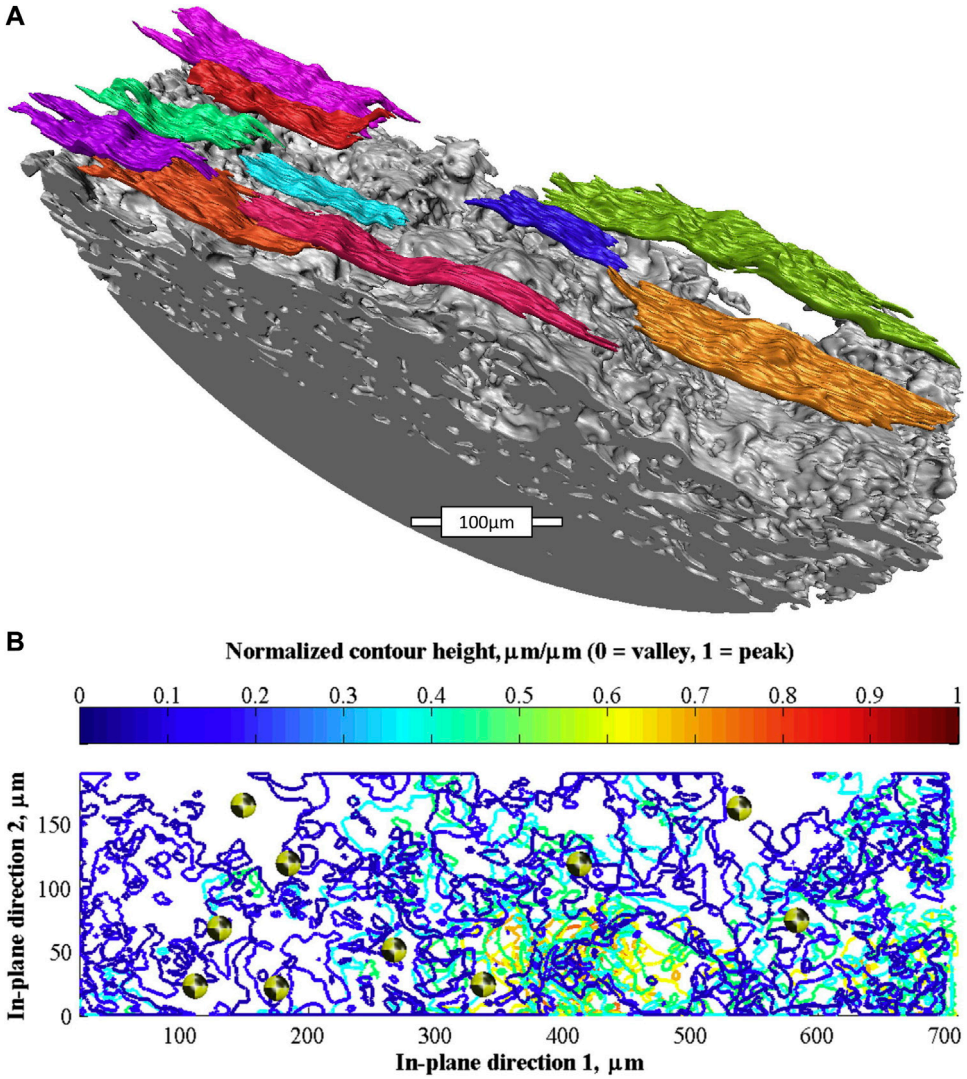

FIGURE 3
X-ray computed tomography (XCT) of an air plasma spray (APS) TBC. **(A)** Segmentation of cracks showing clusters of cracks (colour) with bond coat/substrate (grey). **(B)** Contour map of bond coat surface roughness with centroid of cracked region overlaid (centre mark) for geometry shown in **(A)**. Reprinted from Ahmadian et al. (2015) with permission from Elsevier.

metastable tetragonal phase or cubic phase yttria-stablised zirconia (YSZ) is preferable to avoid the martensitic transformation and the associated unit cell volume change from tetragonal to monoclinic (Kobayashi et al., 1981; Chevalier et al., 2009). Although, rate-dependent with temperature and composition, a heat treatment around and above 1,300°C can also lead to the as-sprayed metastable tetragonal phase decomposing (Stecura, 1985; Miller, 1987; Brandon and Taylor, 1991).

Therefore, the phase stability of a variety of TBC YSZ compositions has widely been studied with XRD (Brandon and Taylor, 1991; Jones, 1997; Witz et al., 2007). However, XRD can misjudge the cubic phase fraction and also the yttria content in the tetragonal phase (Argyriou and Howard, 1995; Ilavsky and Stalick, 2000). Neutron diffraction can provide a more representative estimation with better peak separation between zirconia's tetragonal and cubic phases, although the limited availability of neutron sources restricts its use (Ilavsky and Stalick, 2000; Ilavsky et al., 2001; Kulkarni et al., 2006).

The phase stability of TBC top coat phases can also be changed by interaction with CMAS. The Y^{3+} can diffuse from the metastable tetragonal yttria-stabilised zirconia (t'-YSZ), given the higher solubility of Y^{3+} in CMAS (Nagelberg, 1985). Consequently, this yttrium depleted ZrO_2 can transform upon cooling to the monoclinic phase at 600°C, evaluated by *in situ* variable temperature Raman spectroscopy (Garces et al., 2014). *In situ* techniques are again invaluable in defining the temperature dependence of phase transformations.

CMAS infiltration and reaction with the top coat on small length scales means that TEM is important. For example, the formation of wetting films at grain boundaries and penetration of CMAS glass into inclusions in contact with grain boundaries are seen in EBCs by TEM techniques, such as scanning transmission electron microscopy (STEM), high-angle annular dark-field (HAADF) and

TABLE 1 Overview of techniques characterising the morphology of TBCs and EBCs.

Measurement technique	Application area	Advantages	Disadvantages	Further information (e.g. standards, software and technique-based publications)
Archimedes method	• Global estimate of porosity Lima (2020); Mccormack et al. (2023)	• Simple	• A comparative parameter and only distinguishes between open and closed porosity • Potential for large systematic error due to the assumption about the total sample volume • Minimum pore size relates to the choice of solvent	• Standard Test Methods for Density of Compacted or Sintered Powder Metallurgy (PM) Products Using Archimedes Principle ASTM International, (2013)
Confocal microscopy	• Oxidised TBC bond coat surface morphology Martins et al. (2020)	• Simple (only requires a level sample) • Non-contact	• Limited field of view requires multiple, stitched scans • Requires an exposed surface	• Surface texture parameters - International Organization for Standardization, (2021) • A comparison of surface metrology techniques Conroy et al. (2005)
Electron Backscattered Diffraction (EBSD)	• Grain orientation and texture Chen et al. (2020), Chen et al. (2021)	• Choice of section – cross-section or a particular depth in the coating • Advantageous compared to more subjective intercept or planimetric procedures using the contrast difference from etched SEM or optical micrographs Heyn, (1903); Abrams, (1971); ASTM International, (2021b)	• Only representative of a chosen 2D section • Requires a smooth, level surface, typically achieved by final polishing with colloidal silica • A conductive coating (e.g., Au, Pt or C) may be required to minimise sample charging	• Grain size measurement standard with EBSD International Organization for Standardization, (2020) • Review: Grain and subgrain characterisation by electron backscatter diffraction Humphreys, (2001) • MTEX Open Source Software Bachmann et al. (2010) • AZtecCrystal Processing Software, Oxford Instruments
Mercury Intrusion Porosimetry (MIP)	• Crack healing mechanisms in APS EBC top coats Bakan and Vaßen, (2023)	• Quantify a pore size distribution between 50 nm and 400 µm Rouquerol et al. (2012)	• Only evaluates open porosity • Use of mercury requires adequate safety precautions	• Liquid intrusion and alternative methods for the characterisation of macroporous materials Rouquerol et al. (2012) • BS ISO 15901–1:2016 – Mercury Porosimetry The British Standards Institution, (2016)
Scanning Electron Microscopy (SEM)	• Development of TGO morphology as a function of environment (i.e., time, temperature, steam corrosion) Chen et al. (2008); Richards et al. (2016); Lee, (2018); Ridley et al. (2022) • Steam degradation of EBC top coat Richards et al. (2016); Al Nasiri et al. (2017); Paksoy et al. (2022) • Location of porosity Richards et al. (2016); Bakan and Vaßen, (2022)	• Resolution suitable for many microstructural features such as oxide topography or micron-sized grains • Large field of views with automated stages and stitching of SEM micrographs • Choice of investigated area—cross-section or a particular depth in the coating	• Only representative of a chosen 2D section • Potential for damage from sectioning • A conductive coating (for example, Au, Pt or C) may be required to minimise sample charging	• ASTM: E112-13 Standard Test Methods for Determining Average Grain Size ASTM International, (2021b) • Fiji - Image Analysis software Schindelin et al. (2012) • Image analysis software for TGO examination • AutoTracer Su et al. (2021), CMAT Su et al. (2021) and SOFIA Stack, (2022) • Modelling electron interactions with the CASINO Monte Carlo simulation software Drouin et al. (2007); Demers et al. (2011) • Coating thickness measurement review Giurlani et al. (2020)
X-ray Computed Tomography (XCT)	• Location of internal porosity and cracks Ahmadian et al. (2015); Zhang et al. (2018); Zhu et al. (2018)	• Non-destructive evaluation of 3D geometry of internal porosity	• X-ray attenuation may limit the sample size • Resolution typically limited to features greater than 1 µm Maire and Withers (2014)	• Segmentation software - Avizo, Thermo Fisher Scientific • Techniques for image enhancement and segmentation of porous materials Sheppard et al. (2004) • Porosity segmentation Iassonov et al. (2009)

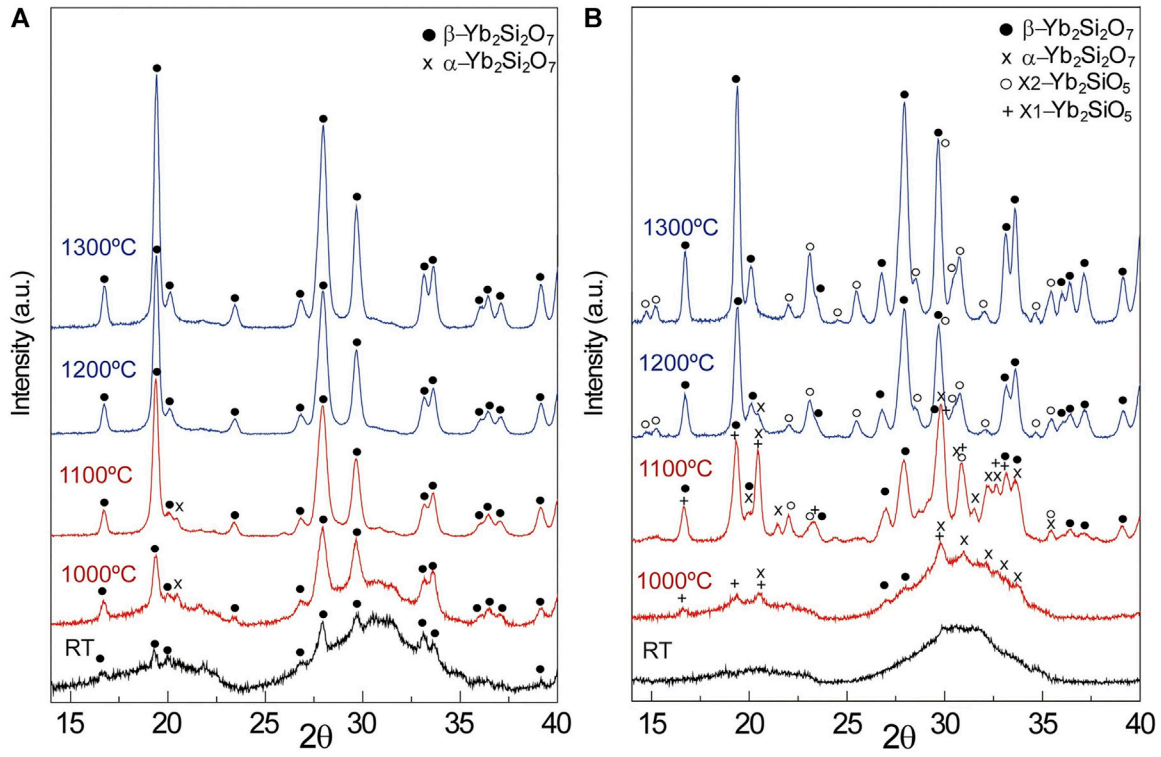

FIGURE 4
X-ray diffraction (XRD) patterns as a function of temperature (RT–Room Temperature, 1,000°C, 1,100°C, 1,200°C, 1,300°C) in air of **(A)** YbDS-3H and **(B)** YbDS-9H. These are two free-standing $Yb_2Si_2O_7$ (YbDS) EBC top coat samples, deposited with different APS processing parameters, with further details in Garcia et al. (2019). Reprinted from Garcia et al. (2021) with permission from Elsevier.

electron energy loss spectroscopy (EELS) (Sternlicht et al., 2022a; Sternlicht et al., 2022b). Complementing this understanding at larger length scales can be XCT, showing a time lapse of CMAS infiltration and the effect of pore morphology (Stolzenburg et al., 2016a; Zhang et al., 2020).

4.2.2 Thermally grown oxide

The formation of a thermally grown oxide (TGO) layer in TBCs and EBCs has seen much attention due to it being a critical failure mechanism. As a result, this has led to many segregation and phase stability studies.

For TBCs, the underlying bond coat affects the TGO phase present. The TGO can contain areas of coarse α-Al_2O_3 (above γ-phase bond coat) and also areas with mixed oxides, consisting of metastable alumina, zirconia and $NiAl_2O_4$ spinel phase (above γ' phase bond coat) (Stiger et al., 1999; Chen et al., 2012; Chen et al., 2022). A pre-oxidation treatment in a low-pressure oxygen environment can suppress the formation of NiO and the $Ni(Cr,Al)_2O_4$ spinel phase by forming α-Al_2O_3, shown with XRD and TEM (Chen et al., 2008a, Chen et al., 2008b; Zhao et al., 2008). However, the depletion of aluminium from α-Al_2O_3 can result in a mixed oxide and spinel TGO after thermal cycling, identified with XRD (Shillington and Clarke, 1999). The formation of these different phases should be avoided to avoid spallation failure of the TBC (Shillington and Clarke, 1999).

Rumpling of the TBC TGO is a roughening of the compressed oxide to relieve its strain energy (Tolpygo and Clarke, 2000). An increased TGO thickness increases this strain energy, and its growth rate can be controlled by reducing the outward diffusion of aluminium with the introduction of rare-earth elements in the bond coat, including rhenium (Bai et al., 2016), yttrium (Chen et al., 2017) and hafnium (Tolpygo and Clarke, 1998). STEM coupled with energy-dispersive X-ray spectroscopy (EDS) can characterise the TGO grain boundary segregation of rare-earth elements, such as yttrium (Chen et al., 2017). The accompanying smaller lateral growth strain of the TGO then resulted in less rumpling (Chen et al., 2017).

A more quantitative measurement of elemental segregation in the TGO requires atom probe tomography (APT) (Miller and Kenik, 2004). Although a sample is typically only representative of a 100 nm region, APT provides unmatched resolution for 3D mapping of elemental segregation (Miller and Kenik, 2004). Such a technique is therefore suitable for fundamental understanding, although sampling many regions of interest as a function of environmental exposure is unrealistic, given the time-consuming nature of sample preparation and experiments.

Figure 5 shows an example of elemental segregation analysed with APT at an α-Al_2O_3 grain boundary (Marquis et al., 2013). The concentration of zirconia and yttrium segregating on the α-Al_2O_3 grain boundary was also shown to increase with proximity to the top coat, suggesting these elements originated from the YSZ top coat (Chen et al., 2022). APT also showed there was preferential segregation towards dislocations (Marquis et al., 2013; Chen et al., 2022). Transmission Kikuchi diffraction (TKD) of needles

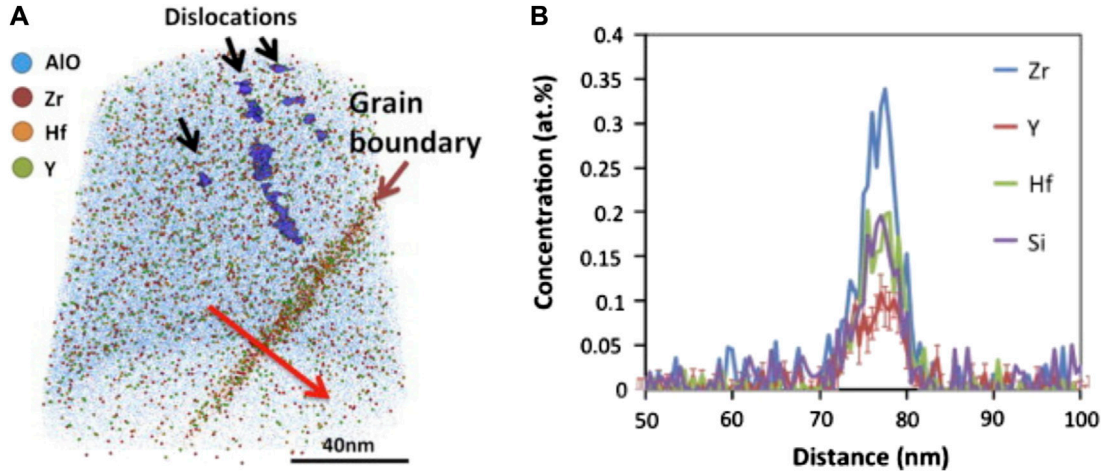

FIGURE 5
(A) Atom probe tomography (APT) reconstruction from an Al_2O_3 TBC TGO layer containing a grain boundary and dislocation lines decorated with Y, Zr, Hf and Si. **(B)** Quantification of atomic concentrations of Zr, Y, Hf and Si at the grain boundary via a concentration profile along the red arrow indicated in **(A)**. Reprinted from Marquis et al. (2013) with permission from Elsevier.

prepared for atom probe tomography also highlighted whether segregation was related to grain boundary misorientation, although no dependence was noted (Chen et al., 2022).

In TBCs, the segregation of sulphur and resulting sulphides reduces the adhesion between the TGO and bond coat due to the different bonding present (Evans et al., 2008). Secondary ion mass spectroscopy (SIMS) and nanoscale secondary ion mass spectroscopy (NanoSIMS) determined the elemental segregation of sulphur at this interface to be up to 10 parts per million, Figure 6 (Bai et al., 2016). These findings highlighted the need for understanding the complete system (i.e. both coating and substrate) given the sulphur was also present in the nickel based superalloy (Lee et al., 1998). A solution to this sulphur segregation was found with the introduction of platinum preferentially gettering the sulphur (Gheno et al., 2010). In addition, glow discharge optical emission spectroscopy (GD-OES) has determined the elemental segregation of sulphur in TBCs given its high depth resolution and capability to detect a variety of elements (Zhao et al., 2017; Lu et al., 2019).

Understanding the crystallinity of the SiO_2 EBC TGO is also important for failure and steam degradation. SIMs studies show that oxygen diffusivity in the amorphous state is five times greater than crystalline β-cristobalite (Lamkin et al., 1992; Rodríguez-Viejo et al., 1993). A crystalline TGO is then expected to be thinner, although a crystalline TGO is commonly reported to cause spallation failure after thermal cycling, due to the 4.5% volume shrinkage that occurs when β-SiO_2 transforms to α-SiO_2 upon cooling (Breneman and Halloran, 2014; Richards et al., 2016).

Identifying the crystalline SiO_2 EBC TGO can be performed with TEM and Raman spectroscopy. Performing selected area electron diffraction (SAED) provides convincing evidence of α-cristobalite at ambient temperature, Figure 7 (Kane et al., 2021). However, TEM requires the time-consuming extraction of a TEM lamella with a limited region of interest. Alternatively, Raman spectroscopy provides a characteristic spectrum of α-cristobalite, without extensive sample preparation, so a crystalline TGO can be identified at several locations (Richards et al., 2015; K; Kane et al., 2021).

SEM and HAADF-STEM are also effective techniques to investigate the effect of top coat composition on TGO chemistry and morphology. For instance, the introduction of Al_2O_3 into EBC top coats can improve their steam corrosion resistance (Lee, 2018; Lee et al., 2021; Paksoy et al., 2022). Such an alumina addition to the top coat results in a reaction layer between the TGO and top coat, which is rich in aluminium and ytterbium, Figure 7 (Lee, 2018; K. A; Kane et al., 2021). The presence of aluminium then reduces the TGO growth rate (Lee, 2018; Lee et al., 2021). Furthermore, during steam testing, the formation of an 80–100 nm ytterbium-aluminium-garnet ($Yb_3Al_5O_{12}$) outer-layer on the top coat prevented transformation of the $Yb_2Si_2O_7$ to Yb_2SiO_5 (Paksoy et al., 2022). The dimensions and phase identification of this layer required TEM studies (Paksoy et al., 2022).

4.2.3 Bond coat

Understanding the TBC bond coat phase transformation of β-(Ni,Pt)Al to γ-(Ni,Pt)Al is important due to the difference in creep deformation. The creep strain rate of β-NiAl is about two orders of magnitude smaller than γ-Ni, so TGO rumpling is more problematic with these β-NiAl bond coats (Noebe et al., 1993; Chen et al., 2017). Furthermore, with the β-(Ni,Pt)Al bond coat, a β to γ phase transformation can occur during thermal cycling due to aluminium depletion (Chen et al., 2017). This β to γ phase transformation occurs above 600°C, evaluated with *in situ* variable temperature XRD (Chen et al., 2015).

Within EBC bond coats, Raman spectroscopy has identified the presence of boron. Boron is typically present in the substrate and can diffuse during thermal treatment (Costello et al., 1981; Lee et al., 2021). The increased asymmetry in the silicon 520.7 cm^{-1} vibrational mode, and additional vibrational mode at 620 cm^{-1} indicate boron is present (Nakano et al., 1992; Knauf et al., 2019; 2020; Rohbeck et al., 2019). These changes to the Raman spectrum suggest boron concentrations above 10^{19} cm^{-3} in the silicon bond coat (Dawber and Elliott, 1963).

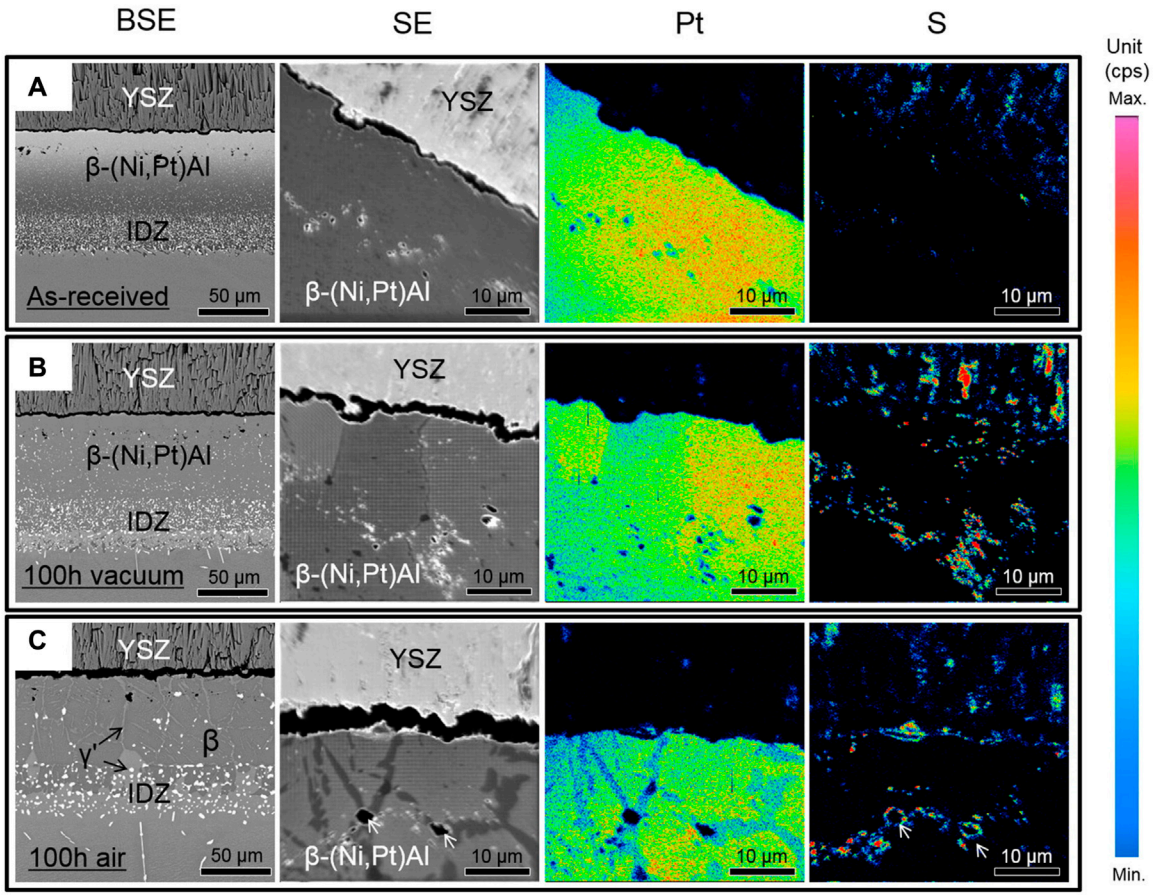

FIGURE 6
Nanoscale secondary ion mass spectrometry (NanoSIMS) mapping of platinum and sulphur on TBC cross-sections with EB-PVD YSZ top coat (Bai et al., 2016). **(A)** As-received with no heat treatment; **(B)** after 100 h at 1,150°C in vacuum and **(C)** after 100 h at 1,150°C in air. From left to right, backscattered electron (BSE) micrograph, and then secondary electron (SE) micrograph with the corresponding platinum and sulphur NanoSIMS maps. The colour scale indicates the counts per second (cps) of 32-S (0–15 cps) and 195-Pt (0–40 cps). Reprinted from Bai et al. (2016) with permission from Elsevier.

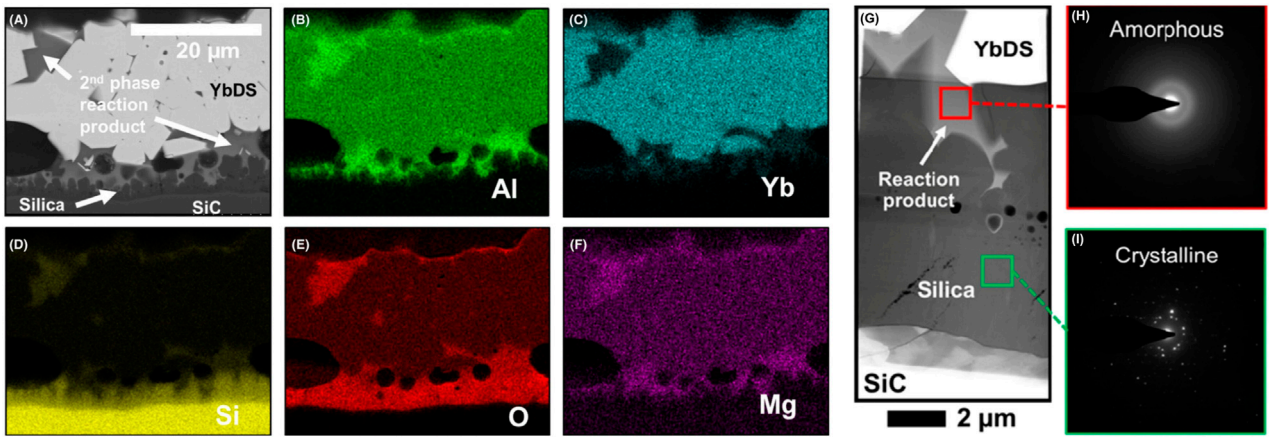

FIGURE 7
Characterising a single layer chemical vapour deposition (CVD) SiC/$Yb_2Si_2O_7$ specimen after 100 h of 1,425°C steam exposure in an alumina reaction tube. **(A)** Cross-sectional backscattered electron micrograph with corresponding **(B)** Al, **(C)** Yb, **(D)** Si, **(E)** O and **(F)** Mg energy-dispersive X-ray spectroscopy (EDS) maps. **(G)** High-angle annular dark-field imaging-scanning transmission electron microscopy (HAADF-STEM) characterising the reaction layer above a silica TGO in the EBC. Selected area electron diffraction (SAED) patterns in the reaction layer **(H)** and silica TGO **(I)**. Reprinted from Kane et al. (2021) with permission from Wiley Materials.

Quantitative light element detection for boron can also be performed with wavelength-dispersive X-ray spectroscopy (WDS) (Lee et al., 2021). Other alternatives include SIMS offering lower boron detection limits (10^{14} cm^{-3} (Ochiai et al., 1980)), and also Inductively Coupled Plasma Mass Spectrometry (ICP-MS) and Glow Discharge Mass Spectroscopy (GDMS), which are more regularly used in semiconductor research fields (Fauveau et al., 2016).

Identifying and quantifying boron concentrations are important as boron increases the rate of oxidation in EBCs (Lee et al., 2021; Lee et al., 2022). Furthermore, the solubility limit of boron at temperature increases, which could also contribute to accelerated oxidation at higher temperatures (Knauf et al., 2020).

4.2.4 Technique overview

Table 2 summarises the techniques informing the chemistry and phase analysis of TBCs and EBCs.

XRD techniques are the most widely used for phase analysis, but limitations in gaining only surface-related information, requiring previously indexed crystalline phases, and difficulty in identifying elements in low concentrations have meant alternatives are required. TEM, coupled with STEM EDS, EELS and HAADF, is a leader in determining elemental segregation to grain boundaries, but can be time consuming if the segregation is inhomogeneous and the location is unknown. On the other hand, APT can offer unmatched 3D spatial resolution for a targeted investigation. Both these techniques suffer in that they are only representative of relatively small samples, and also require expertise in sample preparation, data processing and data analysis.

In this regard, spectroscopy techniques offer a faster alternative and can interrogate larger regions of interest. For example, Raman spectroscopy offers a much simpler identification of phases. WDS is advantageous over EDS in quantitative measurement, although NanoSIMS or glow discharge spectroscopy techniques can detect the low concentrations (i.e. parts per million) needed to identify sulphur segregation in TBCs.

5 Evaluating stress

Evaluating residual stress in TBC and EBC systems is not straightforward given there are multiple layers and defects at different length scales. The TGO, bond coat and top coat can contain processing defects (e.g. porosity, splat boundaries, EB-PVD columns) and multiple phases, resulting in residual stresses from thermal mismatch and elastic mismatch. These microstructures are prone to evolve in-service, and environmental changes, such as the penetration of CMAS or temperature, can also lead to residual stress changes. Such a complex residual stress distribution resulting from microstructures at different length scales, means that multiple evaluation techniques are required (Withers and Bhadeshia, 2001).

The following section outlines characterisation techniques that can evaluate coating strains and stresses in an entire coating system (5.1) and those which are limited to particular coating layers (5.2). Furthermore, techniques determining the thermomechanical properties necessary to evaluate the residual stress, such as the elastic modulus, are described in 5.3.

5.1 Entire coating system

A non-destructive evaluation of strain as a function of coating depth with XRD requires a transmission geometry, typically requiring an intense synchrotron light source. For instance, the measurement of residual strains in TBCs as a function of depth has been performed with heat-treated yttria-stabilised top coats (Li et al., 2016). In this experiment, the evaluated compressive strain reached a maximum about 100 μm from the TGO/bond coat interface, which linked with the likely failure location of TBCs (Li et al., 2016). Further to this experiment, residual strains were measured in as-received and heat treated APS TBC samples, again evaluating compressive strains in the top coat and also tensile strains in the NiCoCrAlY bond coat as a function of depth by synchrotron XRD (Li et al., 2019). With thermal gradients also applied, synchrotron experiments can provide the most representative strain measurements of TBCs and EBCs (Siddiqui et al., 2013).

For EBCs, synchrotron experiments have also yielded strains from Debye ring patterns and consequently evaluated residual stresses in EBCs (Harder et al., 2009; Stolzenburg et al., 2011; 2016b). In combination with *in situ* loading (enabling the determination of elastic constants), and also *in situ* heating, the residual stress distribution was determined throughout the EBC as a function of temperature (Harder et al., 2009; Stolzenburg et al., 2011). Later experiments, then introduced CMAS to perform an *in situ* investigation of molten CMAS with wide-angle X-ray scattering (WAXS) (Stolzenburg et al., 2016b).

Alternatively, a commonly used destructive technique for evaluating stress is the curvature method. A coating and a substrate can develop a curvature, arising from a bending moment in the coating and substrate to satisfy equilibrium. A measurement of the beam displacement can then be used to estimate the residual stress in the coating (Godoy et al., 2002; Hayase et al., 2020). The curvature method has correlated the effect of coating thickness with plasma-sprayed coatings and also the effect of heat treatment on these macro-stresses (Godoy et al., 2002; Hayase et al., 2020).

One mechanism commonly cited as causing residual stress is the thermal mismatch between coating layers. The Stoney equation offers a prediction of these macro-stresses with thermal expansion coefficients evaluated using dilatometry (Stoney, 1909; Richards et al., 2016; Begley and Hutchinson, 2017). Measuring the strain as a function of temperature of bulk samples (i.e. pressed and sintered powders, or free-standing coatings), and assuming isotropic expansion, provides a thermal expansion coefficient representative of a bulk sample (Al Nasiri et al., 2016; Kassem and Al Nasiri, 2021; Ridley et al., 2023).

However, the microstructural complexity of APS and EB-PVD deposited coatings leads to an inhomogeneous residual stress distribution within individual coating layers. For example, between different grain orientations, such as with EB-PVD top coats, or between different phases in the EBC top coat (Withers and Bhadeshia, 2001). XRD is suited to evaluate orientation dependent thermal strains of each phase and using Rietveld

TABLE 2 Overview of techniques informing the chemistry and phase analysis of TBCs and EBCs.

Measurement technique	Application area	Advantages	Disadvantages	Further information (e.g. standards, software and technique-based publications)
Atom Probe Tomography (APT)	• Elemental segregation at TGO grain boundaries Chen et al. (2012); Chen et al. (2022)	• Resolution (<1 nm) • Quantitative elemental measurement for local features • Map elemental distribution in three-dimensions	• Sample preparation to produce sharp needle (~50 nm–150 nm radius) • Only representative of the prepared sample volume	• Review of Atom Probe Tomography Kelly and Miller, (2007) • Review of Atom Probe FIB-Based Specimen Preparation Methods Miller et al. (2007)
Glow Discharge Optical Emission Spectroscopy (GD-OES)	• Elemental segregation in TBCs, including sulphur and hafnium Zhao et al. (2017); Lu et al. (2019)	• High depth resolution (<1 nm) • Low concentration limit • Elemental depth analysis • All elements detectable (including hydrogen)	• Lack of standardisation and reference materials for accuracy calibrations. • Destructive	• Radio-frequency glow discharge spectrometry: A critical review Winchester and Payling, (2004) • Elemental depth profiling of coated and surface-modified materials by GD-OES: hard coatings on cutting tools Wëiss and Marshall, (1997)
Raman Spectroscopy	• SiO_2 TGO crystallinity Kane et al. (2021) • Phase T transformation to monoclinic-ZrO_2 Garces et al. (2014) • Boron detection Nakano et al. (1992); Knauf et al. (2019), Knauf et al. (2020); Rohbeck et al. (2019)	• No extensive sample preparation • Quick, single Raman spectrum data acquisition (seconds/min) • Micrometre resolution - relevant to microstructure variation	• Surface sensitive technique • Unable to penetrate through EBC top coat, must be performed on cross-section for Raman spectra from TGO or bond coat • Experimental parameters specific to phases to avoid fluorescence	• Analysis software - WiRE™ (Renishaw) and LabSpec (HORIBA) • Review of Existing Standards, Guides, and Practices for Raman Spectroscopy Ntziouni et al. (2022)
Scanning Transmission Electron Microscopy (STEM) coupled with Energy-Dispersive X-ray Spectroscopy (EDS), Electron Energy Loss Spectroscopy (EELS) and High-Angle Annular Dark-Field (HAADF)	• Segregation of rare earth elements rhenium Bai et al. (2016), yttrium Chen et al. (2017) and hafnium Tolpygo and Clarke, (1998) • SiO_2 TGO crystallinity Richards et al. (2015); Kane et al. (2021) • γ and γ' phase relationship in TBC bond coat with TGO' Stiger et al. (1999) • CMAS infiltration mechanisms Sternlicht et al. (2022b), Sternlicht et al. (2022a) • $Yb_3Al_5O_{12}$ with alumina present in top coat Paksoy et al. (2022)	• Excellent resolution (<1 nm) Browning and Pennycook, (1995) • Phase identification • Elemental segregation	• Electron transparent sample required. • Only representative of the prepared lamella region • Difficulty in quantifying ytterbium and aluminium given their similar spectral peak positions Lee et al. (2021)	• A review of focused ion beam milling techniques for TEM specimen preparation Giannuzzi and Stevie, (1999) • MC X-ray – Monte Carlo Simulation software for X-ray spectra from electron scattering Gauvin and Michaud, (2009)
Secondary Ion Mass Spectroscopy (SIMS)/Nanoscale Secondary Ion Mass Spectroscopy (NanoSIMS)	• Elemental segregation of sulphur Bai et al. (2016) • Oxygen diffusivity studies Lamkin et al. (1992); Rodríguez-Viejo et al. (1993); Zhao et al. (2020)	• Quantitative analysis with low concentration detection limits (< parts per million) • Light element (H, Li, B) detection possible • Ability to perform oxygen-18 tracer studies • Spatial resolution (down to 50 nm)	• Flat sample required • No information about microstructure • Destructive technique • Limited capability to perform experiments with only a few instruments	• NanoSIMS Review Li et al. (2020)

(Continued on following page)

TABLE 2 (*Continued*) Overview of techniques informing the chemistry and phase analysis of TBCs and EBCs.

Measurement technique	Application area	Advantages	Disadvantages	Further information (e.g. standards, software and technique-based publications)
Transmission Kikuchi Diffraction (TKD)	• Segregation related to grain boundary misorientation Chen et al. (2022)	• Index grain orientations with grain sizes below 100 nm	• Sample preparation required to achieve an electron transparent sample • Only representative of the prepared sample volume	• Using TKD for orientation mapping of nanostructured materials Trimby, (2012) • Transmission EBSD from 10 nm domains Keller and Geiss, (2012)
X-ray Diffraction (XRD)	• Amorphous to crystalline transformation of EBC phases with *in situ* capability Garcia et al. (2021)	• Identify crystalline phases • Simple sample preparation • Applicable to investigating multiple phases simultaneously as experimental parameters not specific to phases	• Surface limited with laboratory X-ray sources • Low concentrations may provide weak signal • Cannot distinguish between composition differences within local areas (i.e. splats in thermally sprayed coatings or columns in EB-PVD coatings)	• Software for refining XRD patterns—GSAS-II Toby and Von Dreele, (2013), Highscore Degen et al. (2014), TOPAS Coelho, (2018) • Guidelines for Rietveld refinement - Mccusker et al. (1999)
	• TBC TGO phase identification Shillington and Clarke, (1999)			
	• TBC top coat phase identification Brandon and Taylor (1991); Stott et al. (1994); Witz et al. (2007)			
	• β to γ phase transformation of β-(Ni,Pt)Al bond coat Chen et al. (2015); Chen et al. (2017)			

refinement has aided the evaluation of anisotropic thermal expansion coefficients of both TBCs (Ochrombel et al., 2010) and EBCs (Salanova et al., 2023).

A targeted evaluation of residual stress can be achieved with the micro-ring core method (μRCM) (Korsunsky et al., 2009; Korsunsky et al., 2010; Zhu et al., 2014). For this technique, a focused ion beam (FIB) or laser mills an incremental annular trench while taking SEM or optical micrographs. Performing digital image correlation (DIC) of these micrographs, can then evaluate the displacement field resulting from strain relief and hence determine the residual

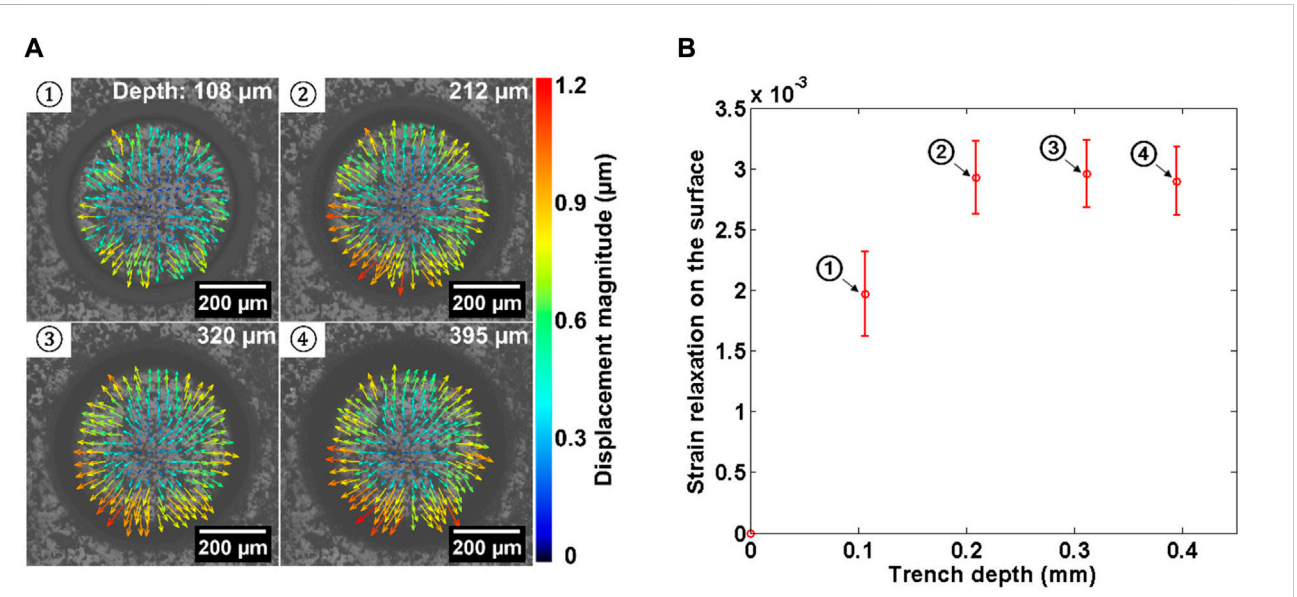

FIGURE 8
Ring core drilling with focused ion beam (FIB) and optical microscopy to evaluate displacement fields with digital image correlation (DIC) of a heat-treated APS TBC sample. **(A)** Depth variation of mapped surface displacements. **(B)** Average surface relief strain evaluated in the pillar's radial direction. Reprinted from Zhang et al. (2019) with permission from Elsevier.

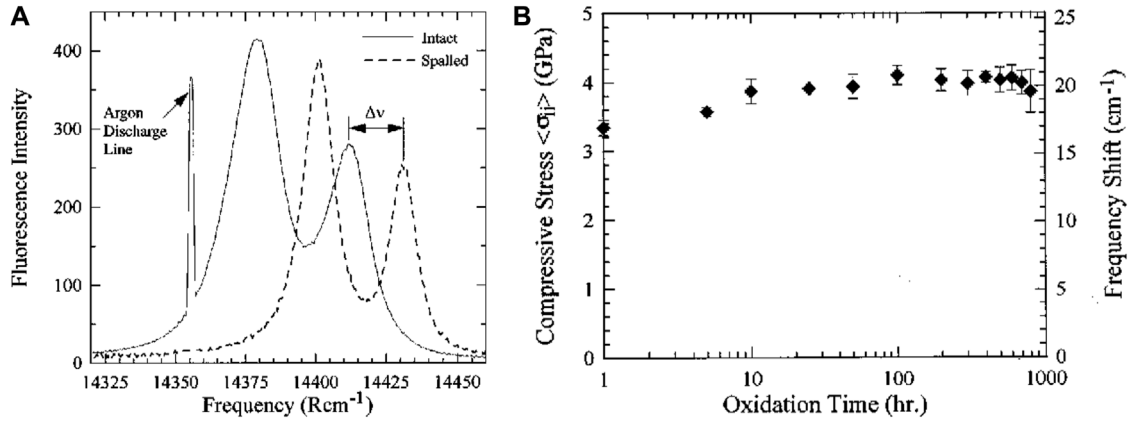

FIGURE 9
(A) Comparison of photoluminescence piezo-spectroscopy (PLPS) profiles from an intact and spalled TBC initially applied on a nickel based superalloy (N5) substrate. **(B)** Evolution of frequency shift with oxidation time at 1,135°C. Reprinted from Christensen et al. (1996) with permission from AIP Publishing.

stress as a function of depth in a coating, Figure 8 (Zhang et al., 2019). The technique is rather intricate, reliant on experimental expertise, and also limited in the investigated region size, so is more likely used to support the findings made by other characterisation techniques.

5.2 Specific layer

Evaluating strains or stresses in a particular coating layer can experimentally be favourable, given some techniques rely upon a characteristic vibrational mode or photon emission. Furthermore, many techniques also have limited penetration depths without access to a synchrotron source.

5.2.1 Thermally grown oxide

The thermally grown oxide layer has seen the most interest in residual stress evaluation given the failure of TBCs and EBCs.

Photoluminescence piezo-spectroscopy (PLPS) has extensively evaluated stresses arising in the α-Al_2O_3 TGO of TBCs (Christensen et al., 1996; Schlichting et al., 2000). The technique is suitable given luminescence (photon emission) arises from the Cr^{3+} impurity in Al_2O_3 and the technique is advantageous because the emitted photons can penetrate through the YSZ top coat in TBCs (Schlichting et al., 2000). The resulting spectroscopy pattern, and the peak's position, asymmetry and intensity are affected by stress, composition and defects (Shillington and Clarke, 1999; Nychka and Clarke, 2001; Selcuk and Atkinson, 2002; Zhao and Xiao, 2006; Wang and Atkinson, 2007). Correlating the peak shift and stress (He and Clarke, 1995) has enabled TBC TGO stress evaluation with PLPS, for example, as a function of top coat thickness (Lima et al., 2017), thermal cycling (Selçuk and Atkinson, 2003), and thermal oxidation time, Figure 9 (Christensen et al., 1996). Figure 9 also highlights that a relative comparison of stress evolution as a function of an environmental condition can improve understanding, even with systematic uncertainties in accurately quantifying the stress (Christensen et al., 1996; Luo and Jones, 2010; Chen et al., 2015).

5.2.2 Bond coat

TBC bond coat strains can be evaluated with the $\sin^2\psi$ technique using oxidised bond coat samples. X-rays can penetrate through a TGO, so stress can be evaluated as a function of oxidation time and temperature. An *in situ* variable temperature $\sin^2\psi$ experiment with a steam oxidised NiCoCrAlY bond coat showed a notable strain change around 600°C (Chen et al., 2015). This indicated the volume expansion from γ-phase to β-phase upon cooling in the NiCoCrAlY bond coat is an important stress contributing mechanism, in addition to the thermal mismatch between TGO and bond coat (Chen et al., 2015).

Stresses in EBC silicon bond coats have been evaluated with Raman spectroscopy using calibrated stress and Raman shift relationships known for silicon (De Wolf, 1996; Rohbeck et al., 2019; Lance et al., 2023). Performing Raman spectroscopy maps across exposed steam degraded silicon samples, has identified shifting of the Raman spectra and associated this with the volume expansion of the SiO_2 α-cristobalite to β-cristobalite phase transformation upon heating (Swainson et al., 2003; Lance et al., 2023).

5.2.3 Top coat

Raman spectroscopy has similarly been used for stress evaluation in the top coat of TBCs. A mapping study showed a correlation between microstructural porosity and Raman peak shift for the 640 cm^{-1} vibrational mode of the t-ZrO_2 phase (Tanaka et al., 2006; Tanaka et al., 2009). Determining local stress is useful to understand how microstructural features affect stress concentrations that may lead to cracking. Stress evaluation studies are lesser performed in the top coats of TBCs and EBCs as the critical failure mechanism involves the bond coat and TGO.

5.3 Thermomechanical performance

Residual stresses are also dependent on thermomechanical properties. The elasticity, plasticity and creep of the coating are

all temperature dependent, and these can all affect the residual stress. Furthermore, the common method of evaluating stress (i.e. using a measurement of strain) relies upon a representative evaluation of other parameters, such as the elastic modulus and Poisson's ratio. As these parameters are influenced by the characterisation technique's sampling volume, the interrogated volume of strain should also match to achieve a reliable evaluation of the stress at the desired length scale. The following section describes techniques to evaluate the elastic-plastic behaviour of the coatings (5.3.1) and also coating creep (5.3.2).

5.3.1 Elastic-plastic behaviour

Microindentation and nanoindentation performed on coating cross-sections are the most common techniques for elastic modulus and hardness evaluation (Zhong et al., 2018; Jang et al., 2020). Applying indentations in this geometry can evaluate the variation in these mechanical properties between adjacent layers and within individual layers. When performed on TBC top coats, this showed a hardness and elastic modulus gradient, with the highest values obtained at the coating's surface (Zhu and Miller, 2000). Furthermore, combining indentation with samples exposed to different sintering durations, showed the effectiveness of the technique in linking the microstructural evolution and the increase in elastic modulus (Zhu and Miller, 2000; Gao et al., 2023).

The elastic modulus of APS TBCs and EBCs can also be assessed with three-point bending. This resulted in a lower elastic modulus value when compared with indentation, which is likely given the more local interaction volume for indentation (Chen et al., 2020).

These scalar representations of elastic modulus evaluated by bending or indentation may be suitable for macroscopic stress evaluation. For example, when combined with a measured strain that is also evaluated from a region of interest that encompasses multiple grains, as with XRD. However, bending or indentation techniques are not very effective in determining anisotropic elastic properties.

Furthermore, following Neumann's Principle, the elastic modulus of TBC and EBC top coat materials is usually anisotropic, given their non-cubic crystal structures (Nye, 1957). Therefore, mechanical properties may be desirable on a much smaller length-scale to determine how APS splat orientation or EB-PVD column orientation affects coating compliance. Consequently, microcantilever bending is considered as an alternative to evaluate the elastic modulus to consider orientation effects. Figure 10 shows microcantilevers with in-plane and out-of-plane orientations (either parallel or normal to the bond coat/top coat interface), and these quantified significant anisotropy resulting from the APS splat morphology (Chen et al., 2019).

As a function of temperature, the plasticity of coating layers also changes. Fundamental studies on single crystals of α-Al_2O_3 show dislocation motion on the basal plane is preferential at high temperatures with prismatic slip preferential under 600°C (Lagerlöf et al., 1994; Mitchell and Heuer, 2005). Therefore, as compressive stresses in the TBC TGO increase, stress relief from dislocation slip may occur at higher temperatures in the α-Al_2O_3 TGO (Chen et al., 2022). The segregation of elements and the temperature dependence of diffusion to these dislocations may also affect dislocation slip (Marquis et al., 2013; Chen et al., 2014).

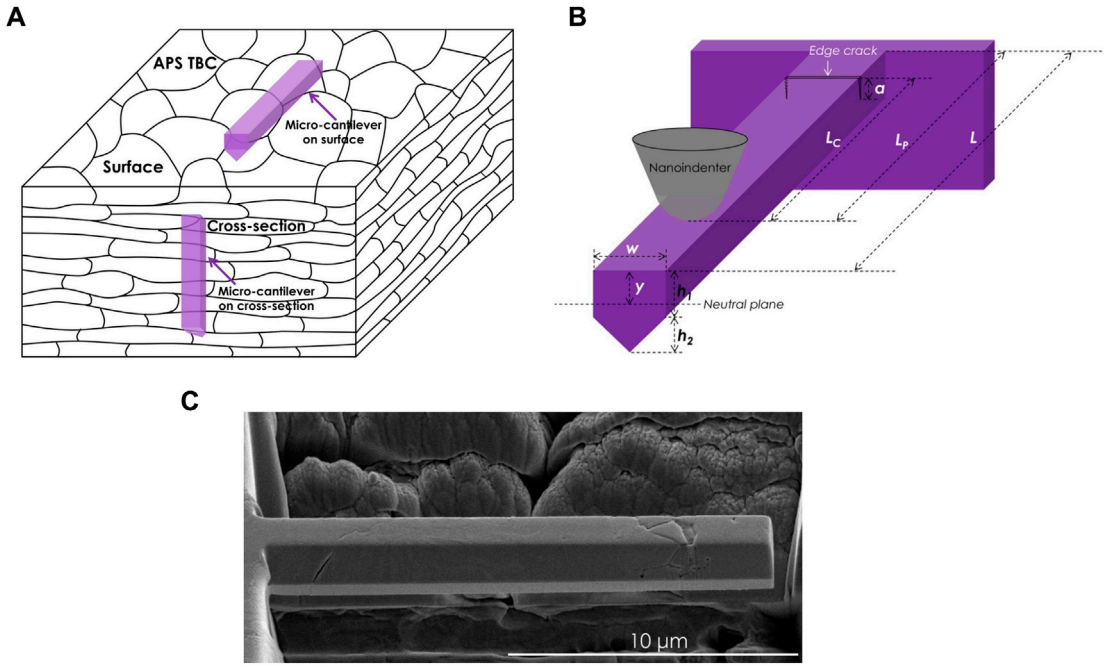

FIGURE 10
Microcantilever beam bending of APS TBC for anisotropic mechanical property evaluation. **(A)** Schematic of the different orientations of the microcantilever beams; **(B)** schematic of testing geometry with nanoindenter to apply load (refer to original publication for description of the labelled parameters); **(C)** Micrograph of a microcantilever beam. Reprinted from Chen et al. (2019) with permission from Elsevier.

5.3.2 Creep

Given the high-temperature operation of TBCs and EBCs, creep deformation (i.e. time dependent strain) can relax the stresses at oxidation temperatures (Evans et al., 2001). Evaluating these strains has been performed with DIC to evaluate a stress exponent for EBCs consistent with diffusional creep (Archer et al., 2020). DIC has also been used with optical images to evaluate the surface displacements and surface strains of a NiCoCrAlY bond coat as a function of temperature (Hemker and Thompson, 2007). The high temperatures required for creep deformation (>700°C) mean that speckle patterns are unstable at these temperatures, so the inherent microstructure is used to track deformation, limiting the correlation ability at the highest resolutions.

Displacement fields can also be evaluated using the intensity contrast in XCT tomographs with digital volume correlation (DVC) (Bay et al., 1999). For example, displacements arising due to TGO growth and bond coat creep can be evaluated at a given temperature and as a function of exposure time (Khoshkhou et al., 2016). However, the microstructure's evolution, such as the sintering of TBC EB-PVD columns and TGO growth, can prevent the same feature being tracked for successful correlation. As a result, there is a time constraint between consecutive tomographs for adequate correlation, which typically requires an intense synchrotron source (Khoshkhou et al., 2016). Furthermore, the voxel size (typically above 1 μm (Maire and Withers, 2014)), also restricts the displacement field's spatial resolution. Techniques with *in situ* mechanical and *in situ* temperature capability, and also better resolution, as achieved with SEM/EBSD (Donoghue 2022; Smith 2022), can further improve the understanding of TBC and EBC deformation.

5.4 Technique overview

Table 3 highlights the techniques evaluating the stress and thermomechanical properties of TBCs and EBCs. Many of these techniques lack a reliable quantitative evaluation of the stress given the dependence on many assumptions of measured strains and linear elastic fracture mechanics. These limitations typically lead to a reliance on qualitative comparison between samples, which may not provide a comprehensive understanding of what causes the relative changes. For instance, while XRD can provide a global measure of the coating strain, it cannot solely detect the relationship between the microstructure and residual stresses. Raman spectroscopy has started to offer insight here, although it relies upon calibration measurements, and spectra require careful interpretation to ensure the peak shift is solely from residual stress.

Synchrotron facilities are an excellent resource for residual stress evaluation, although their availability limits the number of studies performed. Furthermore, the speed of development of TBC and EBC systems means that laboratory-based characterisation techniques are typically favoured to reduce the development cycle time of these industrially relevant coatings. However, synchrotron investigations yield valuable experimental data, unattainable by laboratory systems, and therefore have an important role in comprehensively characterising residual stresses in TBCs and EBCs. In the future, compact light sources using inverse Compton X-ray sources may offer the advantages of synchrotron light sources with increased availability (Gunther et al., 2020).

6 Inducing failure

As described previously, the failure of coatings in the gas-turbine engine environment is complicated. TBCs and EBCs experience residual stresses, oxidation and environmental degradation. The evolving microstructure of the top coat, bond coat and TGO consequently affect the residual stresses and thermomechanical properties to complicate defining the main cause of failure. Therefore, developing accurate models that predict failure behaviour to assess coating lifetime is difficult (Hutchinson and Hutchinson, 2011).

Consequently, experimental techniques that mechanically load and reproduce the in-service failure modes of the coatings are important investigative tools. For example, these techniques can define locations that limit lifetime, while also quantifying the failure (i.e. through measurement of adhesion strength or fracture toughness). Obtaining accurate values for failure related properties can be challenging. Although a relative ranking, for example, with respect to operating conditions, can be combined with an understanding of the morphology, elemental segregation or residual stress discussed previously to understand coating failure.

Tools for inducing failure typically evaluate the coating's adhesion and cohesion. Adhesion refers to the bonding between layers at an interface, while cohesion relates to the integrity of a specific coating layer and how this resists fracture or separation. Both these concepts are crucial for TBCs and EBCs to ensure the coating remains intact and structurally stable under various operating conditions, such as thermal cycling, steam oxidation, and ingested contaminants.

Given these harsh operating conditions and the lifetime limiting failure mechanisms of TBC and EBCs, typically involving cracks propagating along or adjacent to a TGO interface, tools for investigating adhesive failure, rather than cohesive failure, have seen greater use. Furthermore, for TBCs there has been a focus on room-temperature testing, with thermal mismatch contributing to the largest residual stresses, making ambient temperature testing the most relevant for investigating failure (Hutchinson and Hutchinson, 2011).

6.1 Cohesive failure

Investigating cohesive failure considers the inherent fracture resistance of a particular coating layer. Techniques such as XCT, SEM or TEM can all identify initiating defects and crack paths, and from these observations, failure mechanisms can be inferred. However, characterising these cracks occurs without a measurement of the boundary conditions (i.e. displacement or load), making it difficult for a quantitative comparison by evaluating the fracture toughness between coatings exposed to different environments. Therefore, using specific testing geometries, at least with analytical solutions, is favourable to evaluate the fracture toughness.

Additionally, the anisotropic microstructure adds complexity to a representative evaluation of the fracture toughness. As a result, common techniques such as bulk bending tests (i.e. three-point and four-point bending tests) are unsuitable. Therefore, there's a requirement for evaluation of fracture toughness on a scale appropriate to defect size and coating thickness.

TABLE 3 Overview of techniques evaluating the stress and thermomechanical properties of TBCs and EBCs.

Measurement technique	Application area	Advantages	Disadvantages	Further information (e.g. standards, software and technique-based publications)
Curvature method	• Residual stress evaluation Godoy et al. (2002)	• Evaluate macro-stresses	• Substrate stiffness can limit the deflection • Global estimation of stress level (no quantification of surface or interface stresses)	• Stoney equation Stoney, (1909) • Calculation of stress from curvature Brenner and Senderoff, (1949)
Digital Image Correlation (DIC) and Digital Volume Correlation (DVC)	• 3D-displacement field evaluated of thermally grown oxide layer by digital volume correlation Khoshkhou et al. (2016) • Evaluate creep deformation Archer et al. (2020) • Strain measurement of NiCoCrAlY bond coat as a function of temperature Hemker and Thompson, (2007)	• Displacement fields evaluated as a function of temperature	• XCT is limited in resolution for evaluating the displacement field of microstructural features	• Digital volume correlation Bay et al. (1999) • Good practice guide - digital image correlation International Digital Image Correlation Society, (2018)
Dilatometry	• Evaluate thermal expansion coefficients of bulk material Al Nasiri et al. (2016); Kassem and Al Nasiri, (2021); Ridley et al. (2023)	• Representative of a bulk volume	• Evaluates a volumetric thermal expansion coefficient • Sample with parallel sides • Measurement error reduces with increased sample thickness	• ASTM E831 ASTM International, (2014)
Indentation	• Elastic modulus and hardness evaluation Zhu and Miller, (2000); Zhong et al. (2018); Jang et al. (2020)	• Flexible indentation interaction volume dependent on load, indenter size and geometry • Choice of indentation location • Possible to perform multiple indentations on same sample to reduce measurement error	• Evaluates properties with a compressive stress state • Destructive technique to sampled region	• Measurement of hardness and elastic modulus by instrumented indentation Oliver and Pharr, (2004) • Microindentation hardness ASTM E384-22 ASTM International, (2022) • Knoop indentation hardness ASTM C1326-13 ASTM International, (2023) • Vickers indentation hardness - ASTM C1327-15 ASTM International, (2019)
Microcantilever beam bending	• Anisotropy of elastic modulus in APS microstructures Chen et al. (2019)	• Targeted location for elastic modulus evaluation	• Need repeatable sample geometry fabrication • Property evaluation representative of the prepared sample volume	• Mechanical properties of micro-sized copper bending beams machined by the focused ion beam technique Motz et al. (2005)
Micro-ring core method (μRCM)	• Evaluate strain relief as a function of depth Zhang et al. (2019)	• Local technique and can correlate with the microstructure	• Requires intricate geometry • Milling depth, limited by milling technique. Short pulse laser micromachining can mill deeper than FIB	• Residual stress evaluation at the micrometre scale: Analysis of thin coatings by FIB milling and digital image correlation Korsunsky et al. (2010)
Photoluminescence Piezo-spectroscopy (PLPS)	• α-Al_2O_3 stress Christensen et al. (1996); Selçuk and Atkinson, (2003)	• Penetration through YSZ so can perform with top coat present • Micrometre resolution - relevant to microstructure variation	• Method limited to stress evaluation in TBC TGO • Requires calibration between peak shift and stress • Cr^{3+} concentration can also affect peak shift Henderson and Imbusch, (1989); Yu and Clarke, (2002)	• Analysis of Cr^{3+} luminescence spectra Selcuk and Atkinson, (2002) • Determination of the piezospectroscopic coefficients for chromium-doped sapphire He and Clarke, (1995)
Raman Spectroscopy	• t-YSZ top coat stress Tanaka et al. (2006), Tanaka et al. (2009) • Silicon bond coat stress Rohbeck et al. (2019); Lance et al. (2023)	• No extensive sample preparation • Fast Raman spectrum data acquisition (seconds/min) • Micrometre resolution - relevant to microstructure variation	• Surface sensitive technique • Experimental parameters specific to phases to avoid fluorescence • Limited penetration depths prevent stress study from plan-view with EBC top coat present • Requires calibration between peak shift and stress	• Stress measurements in silicon Anastassakis et al. (1970); De Wolf et al. (1996)

(Continued on following page)

TABLE 3 (*Continued*) Overview of techniques evaluating the stress and thermomechanical properties of TBCs and EBCs.

Measurement technique	Application area	Advantages	Disadvantages	Further information (e.g. standards, software and technique-based publications)
X-ray Diffraction (XRD)	• Evaluate the thermal expansion coefficient of TBCs Ochrombel et al. (2010) and EBCs Salanova et al. (2023) • Strain in TBC as a function of depth* Li et al. (2016); Li et al. (2019) • TBC bond coat strains as a function of temperature Chen et al. (2015)	• Non-destructive • Evaluate strains between different phases • Evaluate thermal expansion coefficients dependent on unit cell axes	• *Access to synchrotron source required for through thickness and improved spatial resolution experiments	• Software for Rietveld refinement, listed in Table 1 • CTEAS: determine thermal expansion from high-temperature XRD Jones et al. (2013) • A critical discussion of the $\sin^2(\psi)$ technique Korsunsky, (2008)

As such, Vickers indentations can initiate well-defined radial crack lengths and evaluate fracture toughness (Anstis et al., 1981). Despite challenges posed by non-homogeneous microstructures, such as obtaining Palmqvist cracks from a Vickers indenter in plasma-sprayed microstructures, several studies on TBCs and EBCs have shown consistency with other characterisation techniques (Zhou et al., 2017; Song et al., 2019; Yuan et al., 2022). For example, Mao et al. (2012) conducted a notable study using a modified indentation technique to evaluate fracture toughness and residual stress in plasma sprayed TBCs (Mao et al., 2012). By analysing crack lengths, indentation loads, and deformation patterns, these mechanical properties were load dependent and influenced by both the microstructure and layer thickness.

Another option for fracture toughness evaluation is microcantilever beam bending, Figure 10 (Di Maio and Roberts, 2005; Chen et al., 2019). This provides a local evaluation of the fracture toughness, although the population of defects within the sampled volume can influence the value obtained. For instance, cantilevers manufactured in TBC APS microstructures without splat boundaries, have significantly higher in-plane fracture toughness values (Chen et al., 2019). The ability to machine cantilevers in different regions can also evaluate the fracture toughness variation as a function of depth within the coating (Jaya B et al., 2012). Therefore, it is critical that fracture toughness is evaluated on different length scales to evaluate the impact of different defects contributing to failure, although this is difficult given the inherently inhomogeneous thermal spray microstructure.

6.2 Adhesive failure

Many techniques can investigate a coating's interfacial adhesion. Techniques such as the tensile pull-out test, bending tests (i.e. three or four-point bending) and transverse scratch testing provide good qualitative, comparative understanding of how an in-service environment affects the coating. Other testing methods such as the shear test are also used for quantitative measurement of interfacial properties.

6.2.1 Tensile pull-off and buckle methods

The pull-off test is one of the most widely used tests for comparing the bonding strength between the bond coat/top coat or bond coat/substrate interfaces (Karaoglanli et al., 2013; Ghasemi and Vakilifard, 2017). It involves applying an adhesive bonding agent to attach both sides of the test specimen (i.e. coating and substrate) to a loading fixture. Consequently, a tensile load is applied normal to the coating layer plane. Due to the complex microstructure and composition of both TBCs and EBCs, and also the strength limits of the adhesive agents, multiple tests are required to obtain a statistically significant measure of the coating adhesion or cohesion. Therefore, it is often used for quality control or a qualitative comparison, rather than an accurate quantification of interfacial strength.

The strain to buckle test is commonly used to assess the bonding strength of ceramic coatings (Zhao et al., 2011). This test involves subjecting the coated substrate to a compressive stress until the coating buckles. However, the strain to buckle test has similar limitations to the pull-off test. For example, only a comparative analysis of similar coatings and it also requires many samples. Moreover, the applicability of this technique to EBCs is limited due to the stiffer EBC SiC substrate compared to the nickel based superalloys used with TBCs.

Given these limitations, laser spallation tests have attracted interest. Named the laser shock adhesion test (LASAT), a laser generates shock waves at the substrate or coating surface, and the resulting vibrations can result in delamination at the coating/substrate interface. Although LASAT is currently a rare method for assessing the interfacial properties of TBC or EBCs, its ability to rank different coatings in terms of adhesion, and to evaluate the evolution of adhesion over time with thermal exposure (such as thermal cycling or aging), suggests it has potential for future adoption (Guipont et al., 2019; Maurel et al., 2019; Mahfouz et al., 2023).

6.2.2 Bending tests

Bending tests are also conducted widely for the interfacial fracture behaviour and the bonding strength of TBCs and EBCs. In these tests, a coating is applied to a substrate, and the coated sample is subjected to a bending load with standard testing equipment. The bonding strength of the coating can then be calculated based on the maximum load that the sample withstands before the coating delaminates or fractures.

Bending tests are typically performed with three-point or four-point geometries. In three-point bending, the maximum stress

occurs at the loading point, so a notch is usually manufactured prior to testing, to create a stress concentration at a specific location in the coating thickness, for instance, at the top coat/TGO interface for TBCs (Martins et al., 2021). On the other hand, the four-point bending test involves two loading points and two holding points. This configuration results in a uniform stress between the loading points and results in a larger sample volume under a uniform stress, therefore making the four-point bending geometry more suitable to determining the weakest region of the coating system (Chen et al., 2020).

One example of a four-point bending test that has influenced TBC and EBC development is conducted on the fracture characteristics and damage evolution of coatings with a notch (Zhao et al., 2012; Martins et al., 2021). Using this geometry, the critical strain energy release rate could be linked with the bond coat morphology (previously specified in 4.1.3) to determine preferential bond coat morphologies to resist failure (Martins et al., 2021). Another modified four-point bending geometry can also generate a single interface crack (Zhao et al., 2010). Advantageously, this propagates a crack along the TGO/top coat interface to determine the preferential crack path.

Overall, bending tests have played a significant role in understanding the failure mechanisms and mechanical properties of TBC and EBC systems. They have provided valuable data for modelling the cracking mode, analysing the energy release rate, and developing numerical lifetime models for the durability of these coatings.

6.2.3 Transverse scratch testing

An alternative method evaluating the adhesion strength is transverse scratch testing (Johnstone et al., 1997). Primarily used to investigate APS deposited TBCs, the method involves scratching a polished cross-section with a cone shaped intender under a constant load from the substrate to coating surface. The resulting scratched areas can then evaluate the failure modes (i.e. cohesive or adhesive failure) (Lopez and Beltzung, 1989). While not appropriate for thin EBCs (Al Nasiri et al., 2019; Yilmaz and Xiao, 2022), it is suitable for thicker coatings (i.e. processed using plasma spraying). Studies comparing the technique with the pull-off test suggest it could be useful as a simple and reliable quality control technique (Nohava et al., 2010; Vencl et al., 2011). For example, it has been used to evaluate the effect of heat treatment temperature on TBC bond coat adhesion (Morrell and Rickerby, 1998).

6.2.4 Indentation

Microindentation and nanoindentation techniques can also be used for the analysis of bonding behaviour (Vidakis et al., 2003; Mao et al., 2012). Indentation from the top surface of the coating to evaluate the interfacial toughness is widely used for TBCs (Vasinonta and Beuth, 2001). Cross-sectional indentation at or near the interface has also attracted interest to examine the crack paths and evaluate the interfacial toughness (Lesage and Chicot, 2002; Wang et al., 2012). However, the non-uniform topography of the interfaces resulting from thermal spraying or EB-PVD processing, means that indentation placement is important.

Furthermore, a suitable choice of indenter geometry is required. For example, using indenters with sharp corner geometries (i.e. Vickers and Berkovich) provides an inhomogeneous stress distribution that preferentially initiates cracks near to the corners. Therefore, overcoming this issue is macro-scale spherical indentations near the interface. This generates, large displacements at the interface, with the crack paths examined to determine preferential sites of crack propagation, Figure 11 (Wang et al., 2012).

An appreciation of the residual stresses is also necessary in relationship to the failure test chosen (Clyne and Gill, 1996). All test geometries have an associated sampling volume, which will affect the contribution of residual stresses, and may alter the propagation of a crack (Araujo et al., 2005). Therefore, caution is required when comparing results between different testing geometries.

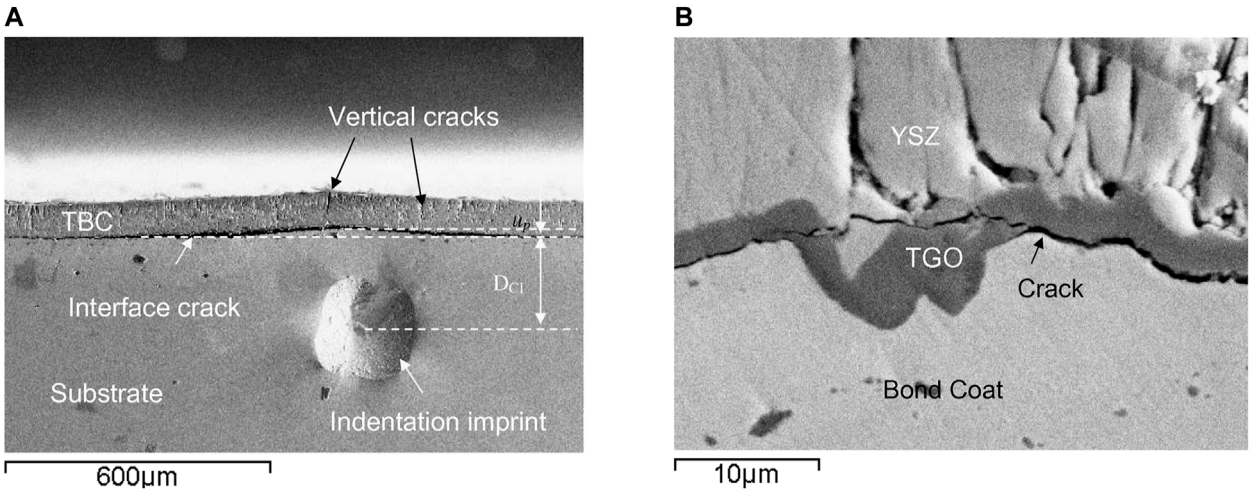

FIGURE 11
(A) Cross-sectional indentation in nickel based superalloy (CMSX4) substrate near TBC interface. **(B)** Resulting crack path along the bond coat/TGO interface. Reprinted from Wang et al. (2012) with permission from Elsevier.

TABLE 4 Overview of techniques used to initiate the failure of TBCs and EBCs.

Measurement technique	Application area	Advantages	Disadvantages	Further information (e.g. standards, software and technique-based publications)
Indentation	• Fracture behaviour of chosen coating location Vasinonta and Beuth, (2001); Wang et al. (2012); Zhou et al. (2017); Song et al. (2019); Yuan et al. (2022)	• Simple and reliable method. • Flexible indentation interaction volume dependent on load, indenter size and geometry • *In situ* capability to obtain intrinsic property measurement	• Properties of local area may not be representative of coating. Therefore, may be insufficient to examine the effect of microstructure or morphology on failure mechanism • Identifying crack lengths can be subjective	• A Critical Evaluation of Indentation Techniques for Measuring Fracture Toughness: I, Direct Crack Measurements Anstis et al. (1981) • Measurement Good Practice Guide No. 9: Palmqvist Toughness for Hard and Brittle Materials Roebuck, (2008)
Laser spallation/Laser shock adhesion test (LASAT)	• Interface strength of TBCs Guipont et al. (2019); Maurel et al. (2019)	• Simple and efficient method for adhesive strength analysis of the coating • Identify weakest part of the coating • Qualitative and quantitative results can be gathered	• Only an evaluation of adhesive strength	• Measurement of interface strength by a laser spallation technique Gupta et al. (1992)
Microcantilever beam bending	• Effect of APS splat boundaries on TBC fracture toughness Chen et al. (2019) • Fracture toughness variation through coating thickness Jaya B et al. (2012); Chen et al. (2021)	• Can be used to examine both cohesive and adhesive strength of the coating • Effect of the texture and microstructure • Site specific evaluation	• Consistent sample preparation requires significant time and expertise required • Prepared sample volume may not be representative	• Measuring fracture toughness of coatings using focused-ion-beam-machined microbeams Di Maio and Roberts, (2005)
Pull off tensile test	• Compare the bonding strength between the bond coat/top coat or bond coat/substrate interface Karaoglanli et al. (2013); Ghasemi and Vakilifard, (2017)	• Simple and reliable method for quality control and comparison • Adhesive and cohesive strength can be distinguished	• Measured strength is limited with the strength of the bonding adhesive agent • High quantity of samples is required • It is not possible to localise the stress (i.e. to coating interface), for specific strength measurement	• ASTM C633-13: Adhesion or Cohesion strength of thermal spray coatings ASTM International, (2021a)
Shear test	• Interfacial adhesion and critical strain energy release rate in EB-PVD TBCs Guo et al. (2005); Guo et al. (2007)	• Mode II loading – can investigate interfacial adhesion and delamination	• Specific test geometry required to apply shear load to the interface	
Three/four-point bending	• Critical strain energy release evaluation in TBCs Martins et al. (2021) • Identify weakest region of the coating system Chen et al. (2020)	• Simple and reliable method for evaluation of cohesive/adhesive bonding strength and fracture toughness • Stress can be localised in to specific section of the coating (i.e. top coat bond coat interface) • *In situ* variable temperature capability possible	• Multiple samples and tests required for statistically significant results • Notching or modified four-bending geometries require additional sample preparation • Not suitable for stiff SiC based substrates	• ASTM C1161-18: Flexural Strength of Advanced Ceramics at Ambient Temperature ASTM International, (2018) • Modified four-point bending specimen preparation Hirakata et al. (2005)
Transverse scratch test	• Scratch test adhesion values for EB-PVD TBC Johnstone et al. (1997); Morrell and Rickerby, (1998)	• Simple and reliable method for evaluation of bonding behaviour qualitatively	• Provides qualitative comparison • Requires suitable coating thickness—typically limited to EB-PVD or APS deposition methods • Initiated cracks can deflect into microcracks	• ISO 27307–2015: Evaluation of adhesion/cohesion of thermal sprayed ceramic coatings by transverse scratch testing International Organization for Standardization, (2015) • The stylus or scratch method for thin film adhesion measurement: some observations and comments Butler et al. (1970)

6.2.5 Shear test

Replicating the in-service mode of failure during testing is important to obtain representative behaviour. In-service, cracks in multi-layered coatings are subject to mixed mode loading (Suo and Hutchinson, 1990; Hutchinson and Suo, 1991; Begley and Hutchinson, 2017). For example, a crack initiated in mode I

(tensile stress normal to the crack) may then propagate into adjacent layers with compressive stress, subjecting these cracks to shear stresses and mode II loading. As a result, the crack changes direction and propagates along an interface which can then lead to coating delamination.

The shear test is a testing geometry with these mode II loading conditions, which lead to delamination failure of TBCs. Although, requiring a specific sample geometry, the shear test has quantified a coating's interfacial adhesion by evaluating the critical strain energy release rate in EB-PVD TBCs (Guo et al., 2005; Guo et al., 2007).

6.3 Technique overview

Table 4 contains an array of techniques for initiating the failure of TBCs and EBCs, and details their advantages and disadvantages. Even though some techniques have been standardised by industrial stakeholders performing TBC and EBC research and development (i.e. pull off test, *etc.*), obtaining reliable results to understand failure has proven a difficult feat, given the size and geometry of the coatings. Furthermore, the actual failure of TBCs and EBCs often occurs due to residual stresses evolving in environmental conditions for extended periods, such as thermal cycling or high-temperature steam oxidation. Therefore, work is still needed to ensure in-service failure modes are reproduced with failure testing that is effective and efficient.

7 Conclusion

Characterisation techniques facilitate the understanding of thermal barrier coating and environmental barrier coating failure by revealing the evolution of microstructure, residual stresses and thermomechanical properties throughout their lifetime. All these factors contribute to coating performance; an appreciation of each factor and their interconnections is crucial to successful coating development. This understanding, in combination with techniques to initiate failure, can then inform of desirable microstructures and compositions to improve coating performance and prolong coating lifetime.

A wide variety of characterisation techniques are presented for investigating thermal barrier coating and environmental barrier coating failure. While the understanding of coating performance is complex, it is essential that the advantages and disadvantages of characterisation techniques in respect to thermal barrier coatings and environmental barrier coatings are also understood. This enables the effective choice of a combination of techniques to investigate these coatings on a variety of length scales.

The need for characterising thermal barrier coatings and environmental barrier coatings will only grow into the future. Improving the efficiency and lowering the environmental impact of gas-turbine engines remains desirable, and consequently this requires substrates and coatings to operate in increasingly extreme environments. Therefore, understanding coating failure will continue to rely upon characterisation techniques to further develop high-performance thermal barrier coatings and environmental barrier coatings.

Author contributions

DS: Writing–original draft, Writing–review and editing. AP: Writing–original draft, Writing–review and editing. PX: Funding acquisition, Project administration, Supervision, Writing–review and editing, Conceptualization, Resources.

Funding

The author(s) declare financial support was received for the research, authorship, and/or publication of this article. DS acknowledges funding support from the Engineering and Physical Sciences Research Council (EPSRC) Doctoral Training Partnership (DTP) (grant number EP/R513131/1).

Acknowledgments

PX would like to acknowledge support from the Royal Academy of Engineering and Rolls-Royce for the appointment of Rolls-Royce/Royal Academy of Engineering Research Chair in Advanced Coating Technology.

Conflict of interest

The authors declare that the research was conducted in the absence of any commercial or financial relationships that could be construed as a potential conflict of interest.

Publisher's note

All claims expressed in this article are solely those of the authors and do not necessarily represent those of their affiliated organizations, or those of the publisher, the editors and the reviewers. Any product that may be evaluated in this article, or claim that may be made by its manufacturer, is not guaranteed or endorsed by the publisher.

References

Abrams, H. (1971). Grain size measurement by the intercept method. *Metallography* 4 (1), 59–78. doi:10.1016/0026-0800(71)90005-X

Ahmadian, S., Browning, A., and Jordan, E. H. (2015). Three-dimensional X-ray micro-computed tomography of cracks in a furnace cycled air plasma sprayed thermal barrier coating. *Scr. Mater.* 97, 13–16. doi:10.1016/J.SCRIPTAMAT.2014.10.026

Al Nasiri, N., Patra, N., Horlait, D., Jayaseelan, D. D., and Lee, W. E. (2016). Thermal properties of rare-earth monosilicates for EBC on Si-based ceramic composites. *Am. Ceram. Soc.* 99 (2), 589–596. doi:10.1111/jace.13982

Al Nasiri, N., Patra, N., Jayaseelan, D., and Lee, W. (2017). Water vapour corrosion of rare earth monosilicates for environmental barrier coating application. *Ceram. Int.* 43 (10), 7393–7400. doi:10.1016/j.ceramint.2017.02.123

Al Nasiri, N., Patra, N., Pezoldt, M., Colas, J., and Lee, W. (2019). Investigation of a single-layer EBC deposited on SiC/SiC CMCs: processing and corrosion behaviour in high-temperature steam. *J. Eur. Ceram. Soc.* 39, 2703–2711. doi:10.1016/j.jeurceramsoc.2018.12.019

Anastassakis, E., Pinczuk, A., Burstein, E., Pollak, F., and Cardona, M. (1970). Effect of static uniaxial stress on the Raman spectrum of silicon. *Solid State Commun.* 8, 1053–1058. doi:10.1016/0038-1098(93)90294-W

Anstis, G. R., Chantikul, P., Lawn, B., and Marshall, D. (1981). A critical evaluation of indentation techniques for measuring fracture toughness: I, direct crack measurements. *J. Am. Ceram. Soc.* 64 (9), 533–538. doi:10.1111/J.1151-2916.1981.TB10320.X

Anton, R., Leisner, V., Watermeyer, P., Engstler, M., and Schulz, U. (2020). Hafnia-doped silicon bond coats manufactured by PVD for SiC/SiC CMCs. *Acta Mater.* 183, 471–483. doi:10.1016/j.actamat.2019.10.050

Araujo, P., Chicot, D., Staia, M., and Lesage, J. (2005). Residual stresses and adhesion of thermal spray coatings. *Surf. Eng.* 21 (1), 35–40. doi:10.1179/174329405X30020

Archer, T., Berny, M., Beauchêne, P., and Hild, F. (2020). Creep behavior identification of an environmental barrier coating using full-field measurements. *J. Eur. Ceram. Soc.* 40 (15), 5704–5718. doi:10.1016/j.jeurceramsoc.2020.06.009

Argyriou, D. N., and Howard, C. J. (1995). Re-Investigation of yttria-tetragonal zirconia polycrystal (Y-TZP) by neutron powder diffraction-a cautionary tale. *J. Appl. Cryst.* 28, 206–208. doi:10.1107/s0021889894011015

ASTM International (2013). *ASTM B962 – 17 standard test methods for density of compacted or sintered powder metallurgy (PM) products using archimedes Principle*. ASTM B962-17. 10.1520/B0962-17.2.

ASTM International (2014). *ASTM E831-14 standard test method for linear thermal expansion of solid materials by thermomechanical analysis*. doi:10.1520/E0831-06

ASTM International (2018). *ASTM C1161-18 standard test method for flexural strength of advanced ceramics at ambient temperature*. doi:10.1520/C1161-18R23

ASTM International (2019). *ASTM C1327-15 standard test method for Vickers indentation hardness of advanced ceramics*. doi:10.1520/C1327-15R19

ASTM International (2021a). *ASTM C633–13 standard test method for adhesion or cohesion strength of thermal spray coatings*. doi:10.1520/C0633-13R21

ASTM International (2021b). *ASTM E112-13 standard test methods for determining average grain size*. doi:10.1520/E0112-13R21

ASTM International (2022). *ASTM E384-22 standard test method for microindentation hardness of materials*. doi:10.1520/E0384-22

ASTM International (2023). *ASTM C1326-13 standard test method for knoop indentation hardness of advanced ceramics*. doi:10.1520/C1326-13R18

Bachmann, F., Hielscher, R., and Schaeben, H. (2010). Texture analysis with MTEX – free and open source software toolbox. *Solid State Phenom.* 160, 63–68. doi:10.4028/WWW.SCIENTIFIC.NET/SSP.160.63

Bai, M., Jian, H., and Chen, J. (2016). Migration of sulphur in thermal barrier coatings during heat treatment. *Materials & Design* 97. doi:10.1016/j.matdes.2016.02.109

Bakan, E., and Vaßen, R. (2017). Ceramic top coats of plasma-sprayed thermal barrier coatings: materials, processes, and properties. *J. Therm. Spray Technol.* 26 (6), 992–1010. doi:10.1007/s11666-017-0597-7

Bakan, E., and Vaßen, R. (2022). Oxidation kinetics of atmospheric plasma sprayed environmental barrier coatings. *J. Eur. Ceram. Soc.* 42 (12), 5122–5128. doi:10.1016/J.JEURCERAMSOC.2022.05.003

Bakan, E., and Vaßen, R. (2023). Crack healing mechanisms in atmospheric plasma sprayed Yb-silicate coatings during post-process heat treatment. *J. Eur. Ceram. Soc.* 43 (8), 3684–3693. doi:10.1016/j.jeurceramsoc.2023.02.005

Bay, B. K., Smith, T. S., Fyhrie, D. P., and Saad, M. (1999). Digital volume correlation: three-dimensional strain mapping using X-ray tomography. *Exp. Mech.* 39 (3), 217–226. doi:10.1007/BF02323555

Begley, M. R., and Hutchinson, J. W. (2017). The mechanics and reliability of films, multilayers and coatings. *Multilayers Coatings*, 1–288. doi:10.1017/9781316443606

Bhatt, R. T., Choi, S. R., Cosgriff, L. M., Fox, D. S., and Lee, K. N. (2008). Impact resistance of environmental barrier coated SiC/SiC composites. *Mater. Sci. Eng. A* 476, 8–19. doi:10.1016/j.msea.2007.04.067

Borom, M. P., Johnson, C. A., and Peluso, L. A. (1996). Role of environment deposits and operating surface temperature in spallation of air plasma sprayed thermal barrier coatings. *Surf. Coatings Technol.* 86, 116–126. doi:10.1016/S0257-8972(96)02994-5

Brandon, J. R., and Taylor, R. (1991). Phase stability of zirconia-based thermal barrier coatings Part I. Zirconia-yttria alloys. *Surf. Coatings Technol.* 46, 75–90. doi:10.1016/0257-8972(91)90151-L

Breneman, R. C., and Halloran, J. W. (2014). Stress development and fracture of surface nucleated cristobalite on silica glass. *J. Am. Ceram. Soc.* 97 (11), 3483–3488. doi:10.1111/JACE.13181

Brenner, A., and Senderoff, S. (1949). Calculation of stress in electrodeposits from the curvature of a plated strip. *J. Res. Natl. Bureau Stand.* 42 (2), 105. doi:10.6028/JRES.042.009

Browning, N. D., and Pennycook, S. J. (1995). Atomic-resolution electron energy-loss spectroscopy in the scanning transmission electron microscope. *J. Microsc.* 180 (3), 230–237. doi:10.1111/J.1365-2818.1995.TB03682.X

Butler, D. W., Stoddart, C. T. H., and Stuart, P. R. (1970). The stylus or scratch method for thin film adhesion measurement: some observations and comments. *J. Phys. D Appl. Phys.* 3, 877–883. doi:10.1088/0022-3727/3/6/307

Cao, G., Wang, Y. H., Ding, Z. Y., Liu, Z. G., Ouyang, J. H., Wang, Y. M., et al. (2021). CMAS hot corrosion behavior of rare-earth silicates for environmental barrier coatings applications: a comprehensive review. *Heat Treat. Surf. Eng.* 3 (1), 9–28. doi:10.1080/25787616.2021.2019389

Chen, W. R., Archer, R., Huang, X., and Marple, B. (2008a). TGO growth and crack propagation in a thermal barrier coating. *J. Therm. Spray Technol.* 17 (5–6), 858–864. doi:10.1007/s11666-008-9251-8

Chen, W. R., Wu, X., Marple, B., Lima, R., and Patnaik, P. (2008b). Pre-oxidation and TGO growth behaviour of an air-plasma-sprayed thermal barrier coating. *Surf. Coatings Technol.* 202 (16), 3787–3796. doi:10.1016/J.SURFCOAT.2008.01.021

Chen, Y., Li, C., Zhao, X., and Xiao, P. (2020). Measurements and understanding of the stiffness of an air plasma sprayed thermal barrier coating. *Surf. Coatings Technol.* 394, 125678. doi:10.1016/j.surfcoat.2020.125678

Chen, Y., Reed, R. C., and Marquis, E. A. (2012). As-coated thermal barrier coating: structure and chemistry. *Scr. Mater.* 67, 779–782. doi:10.1016/j.scriptamat.2012.06.023

Chen, Y., Reed, R. C., and Marquis, E. A. (2014). Interfacial solute segregation in the thermally grown oxide of thermal barrier coating structures. *Oxid. Metals* 82 (5–6), 457–467. doi:10.1007/s11085-014-9502-7

Chen, Y., Rice, K. P., Prosa, T. J., Reed, R. C., and Marquis, E. A. (2022). Al2O3 grain boundary segregation in a thermal barrier coating on a Ni-based superalloy. *Microsc. Microanal.* 28 (5), 1453–1462. doi:10.1017/S1431927622000678

Chen, Y., Zhang, X., Williams, C. J., Brewster, G., and Xiao, P. (2021). Determination of fracture toughness of a platinum-modified nickel aluminide coating by micromechanical testing. *Materialia* 20, 101267. doi:10.1016/J.MTLA.2021.101267

Chen, Y., Zhang, X., Zhao, X., Markocsan, N., Nylén, P., and Xiao, P. (2019). Measurements of elastic modulus and fracture toughness of an air plasma sprayed thermal barrier coating using micro-cantilever bending. *Surf. Coatings Technol.* 374, 12–20. doi:10.1016/j.surfcoat.2019.05.031

Chen, Y., Zhao, X., Bai, M., Yang, L., and Wang, L. (2017). A mechanistic understanding on rumpling of a NiCoCrAlY bond coat for thermal barrier coating applications. *Acta Mater.* 128, 31–42. doi:10.1016/J.ACTAMAT.2017.02.003

Chen, Y., Zhao, X., Dang, Y., Xiao, P., Curry, N., Markocsan, N., et al. (2015). Characterization and understanding of residual stresses in a NiCoCrAlY bond coat for thermal barrier coating application. *Acta Mater.* 94, 1–14. doi:10.1016/j.actamat.2015.04.053

Chevalier, J., Gremillard, L., Virkar, A. V., and Clarke, D. R. (2009). The tetragonal-monoclinic transformation in zirconia: lessons learned and future trends. *J. Am. Ceram. Soc.* 92 (9), 1901–1920. doi:10.1111/j.1551-2916.2009.03278.x

Christensen, R. J., Lipkin, D. M., Clarke, D. R., and Murphy, K. (1996). Nondestructive evaluation of the oxidation stresses through thermal barrier coatings using Cr3+ piezospectroscopy. *Appl. Phys. Lett.* 69 (24), 3754–3756. doi:10.1063/1.117182

Clarke, D. R., Oechsner, M., and Padture, N. P. (2012). Thermal-barrier coatings for more efficient gas-turbine engines. *MRS Bull.* 37 (10), 891–898. doi:10.1557/mrs.2012.232

Clyne, T. W., and Gill, S. C. (1996). Residual stresses in thermal spray coatings and their effect on interfacial adhesion: a review of recent work. *J. Therm. Spray Technol.* 5 (4), 401–418. doi:10.1007/BF02645271

Coelho, A. A. (2018). *TOPAS* and *TOPAS-Academic*: an optimization program integrating computer algebra and crystallographic objects written in C++. *J. Appl. Crystallogr.* 51 (1), 210–218. doi:10.1107/S1600576718000183

Conroy, M., Armstrong, J., and Hobson, T. (2005). A comparison of surface metrology techniques. *J. Phys. Conf. Ser.* 13 (1), 458–465. doi:10.1088/1742-6596/13/1/106

Costello, J. A., Tressler, R. E., and Tsong, I. S. T. (1981). Boron redistribution in sintered α-SiC during thermal oxidation. *J. Am. Ceram. Soc.* 64 (6), 332–335. doi:10.1111/J.1151-2916.1981.TB10298.X

Czech, N., Fietzek, H., Juez-Lorenzo, M., Kolarik, V., and Stamm, W. (1999). Studies of the bond-coat oxidation and phase structure of TBCs. *Surf. Coatings Technol.* 113 (1–2), 157–164. doi:10.1016/S0257-8972(98)00835-4

Dawber, P. G., and Elliott, R. J. (1963). Theory of optical absorption by vibrations of defects in silicon. *Proc. Phys. Soc.* 81, 453–460. doi:10.1088/0370-1328/81/3/309

Deal, B. E., and Grove, A. S. (1965). General relationship for the thermal oxidation of silicon. *J. Appl. Phys.* 36 (12), 3770–3778. doi:10.1063/1.1713945

Degen, T., Sadki, M., Bron, E., König, U., and Nénert, G. (2014). The HighScore suite. *Powder Diffr.* 29, S13–S18. doi:10.1017/S0885715614000840

Demers, H., Poirier-Demers, N., Couture, A. R., Joly, D., Guilmain, M., de Jonge, N., et al. (2011). Three-Dimensional electron microscopy simulation with the CASINO Monte Carlo software. *J. Scanning Microsc.* 33 (3), 135–146. doi:10.1002/sca.20262

Desai, P. D. (1986). Thermodynamic properties of iron and silicon. *J. Phys. Chem. Reference Data* 15 (3), 967–983. doi:10.1063/1.555761

De Wolf, I. (1996). Micro-Raman spectroscopy to study local mechanical stress in silicon integrated circuits. *Semicond. Sci. Technol.* 11, 139–154. doi:10.1088/0268-1242/11/2/001

De Wolf, I., Maes, H. E., and Jones, S. K. (1996). Stress measurements in silicon devices through Raman spectroscopy: bridging the gap between theory and experiment. *J. Appl. Phys.* 79, 7148–7156. doi:10.1063/1.361485

Di Maio, D., and Roberts, S. G. (2005). Measuring fracture toughness of coatings using focused-ion-beam-machined microbeams. *J. Mater. Res.* 20 (2), 299–302. doi:10.1557/JMR.2005.0048

Donoghue, J. M. (2022). "Integration of EBSD acquisition into fully automated *in-situ* thermo-mechanical testing for high temporal and spatial resolution," in 16th Multinational Congress on Microscopy (MCM16), Brno, 4th-9th 2022.

Drouin, D., Couture, A. R., Joly, D., Tastet, X., Aimez, V., and Gauvin, R. (2007). CASINO V2.42—a fast and easy-to-use modeling tool for scanning electron microscopy and microanalysis users. *Scanning* 29 (3), 92–101. doi:10.1002/SCA.20000

Eaton, H. E., et al. (2000). "EBC protection of SiC/SiC composites in the gas turbine combustion environment," in ASME Turbo Expo 2000: Power for Land, Sea, and Air, New Orleans, Louisiana, USA, June 4–7, 2001. doi:10.1115/2000-GT-0631

Eaton, H. E., and Linsey, G. D. (2002). Accelerated oxidation of SiC CMCs by water vapor and protection via environmental barrier coating approach. *J. Eur. Ceram. Soc.* 22, 2741–2747. doi:10.1016/S0955-2219(02)00141-3

Evans, A. G., Clarke, D. R., and Levi, C. G. (2008). The influence of oxides on the performance of advanced gas turbines. *J. Eur. Ceram. Soc.* 28 (7), 1405–1419. doi:10.1016/j.jeurceramsoc.2007.12.023

Evans, A. G., He, M. Y., and Hutchinson, J. W. (2001). Mechanics-based scaling laws for the durability of thermal barrier coatings. *Prog. Mater. Sci.* 46 (3–4), 249–271. doi:10.1016/S0079-6425(00)00007-4

Evans, A. G., and Hutchinson, J. W. (1984). On the mechanics of delamination and spalling in compressed films. *Int. J. Solids Struct.* 20 (5), 455–466. doi:10.1016/0020-7683(84)90012-X

Evans, A. G., and Hutchinson, J. W. (1995). The thermomechanical integrity of thin films and multilayers. *Acta Metallurgica Materialia* 43 (7), 2507–2530. doi:10.1016/0956-7151(94)00444-M

Evans, A. G., and Hutchinson, J. W. (2007). The mechanics of coating delamination in thermal gradients. *Surf. Coatings Technol.* 201, 7905–7916. doi:10.1016/j.surfcoat.2007.03.029

Evans, A. G., Mumm, D., Hutchinson, J., Meier, G., and Pettit, F. (2001). Mechanisms controlling the durability of thermal barrier coatings. *Prog. Mater. Sci.* 46, 505–553. doi:10.1016/S0079-6425(00)00020-7

Fang, Q., Sidky, P. S., and Hocking, M. G. (1999). Erosion and corrosion of PSZ-zirconia and the t–m phase transformation. *Wear* 233–235, 615–622. doi:10.1016/S0043-1648(99)00239-2

Fauveau, A., et al. (2016). "Comparison of characterization techniques for measurements of doping concentrations in compensated n-type silicon," in *Energy procedia* (Amsterdam, Netherlands: Elsevier Ltd), 691–696. doi:10.1016/j.egypro.2016.07.045

Fernandez-Carrion, A. J., Allix, M., and Becerro, A. I. (2013). Thermal expansion of rare-earth pyrosilicates. *J. Am. Ceram. Soc.* 96 (7), 2298–2305. doi:10.1111/jace.12388

Fleck, N. A., Cocks, A. C. F., and Lampenscherf, S. (2014). Thermal shock resistance of air plasma sprayed thermal barrier coatings. *J. Eur. Ceram. Soc.* 34, 2687–2694. doi:10.1016/j.jeurceramsoc.2014.01.002

Gao, Z., Zhang, X., Chen, Y., Chalk, C., Nicholls, J., Brewster, G., et al. (2023). Strain tolerance evolution of EB-PVD TBCs after thermal exposure or CMAS attack. *J. Eur. Ceram. Soc.* 44, 426–434. [Preprint]. doi:10.1016/j.jeurceramsoc.2023.08.047

Garces, H. F., Senturk, B. S., and Padture, N. P. (2014). *In situ* Raman spectroscopy studies of high-temperature degradation of thermal barrier coatings by molten silicate deposits. *Scr. Mater.* 76, 29–32. doi:10.1016/j.scriptamat.2013.12.008

Garcia, E., Garces, H. F., Turcer, L. R., Bale, H., Padture, N. P., and Sampath, S. (2021). Crystallization behavior of air-plasma-sprayed ytterbium-silicate-based environmental barrier coatings. *J. Eur. Ceram. Soc.* 41 (6), 3696–3705. doi:10.1016/J.JEURCERAMSOC.2020.12.051

Garcia, E., Lee, H., and Sampath, S. (2019). Phase and microstructure evolution in plasma sprayed Yb2Si2O7 coatings. *J. Eur. Ceram. Soc.* 39 (1), 1477–1486. doi:10.1016/j.jeurceramsoc.2018.11.018

Gauvin, R., and Michaud, P. (2009). MC X-Ray, a new Monte Carlo program for quantitative X-ray microanalysis of real materials. *Microsc. Microanal.* 15 (Suppl. 2), 488–489. doi:10.1017/S1431927609092423

Ghasemi, R., and Vakilifard, H. (2017). Plasma-sprayed nanostructured YSZ thermal barrier coatings: thermal insulation capability and adhesion strength. *Ceram. Int.* 43 (12), 8556–8563. doi:10.1016/j.ceramint.2017.03.074

Gheno, T., Monceau, D., Oquab, D., and Cadoret, Y. (2010). Characterization of sulfur distribution in Ni-based superalloy and thermal barrier coatings after high temperature oxidation: a SIMS analysis. *Oxid. Metals* 73 (1–2), 95–113. doi:10.1007/S11085-009-9164-Z

Ghosh, S. (2015). "Thermal barrier ceramic coatings — a review," in *Advanced ceramic processing* (Kolkata, India: InTech), 111–138. doi:10.5772/61346

Giannuzzi, L. A., and Stevie, F. A. (1999). A review of focused ion beam milling techniques for TEM specimen preparation. *Micron* 30, 197–204. doi:10.1016/S0968-4328(99)00005-0

Gil, A., Shemet, V., Vassen, R., Subanovic, M., Toscano, J., Naumenko, D., et al. (2006). Effect of surface condition on the oxidation behaviour of MCrAlY coatings. *Surf. Coatings Technol.* 201 (7), 3824–3828. doi:10.1016/j.surfcoat.2006.07.252

Giurlani, W., Berretti, E., Innocenti, M., and Lavacchi, A. (2020). Measuring the thickness of metal coatings: a review of the methods. *Coatings* 10 (12), 1211–1236. doi:10.3390/coatings10121211

Godoy, C., Souza, E., Lima, M., and Batista, J. (2002). Correlation between residual stresses and adhesion of plasma sprayed coatings: effects of a post-annealing treatment. *Thin Solid Films* 420 (421), 438–445. doi:10.1016/S0040-6090(02)00805-2

Gohardani, O. (2011). Impact of erosion testing aspects on current and future flight conditions. *Prog. Aerosp. Sci.* 47 (4), 280–303. doi:10.1016/j.paerosci.2011.04.001

Gopal Thakare, J., Pandey, C., Mahapatra, M. M., and Mulik, R. S. (2021). Thermal barrier coatings—a state of the art review. *Therm. Barrier Coatings-A State Art Rev.* 27, 1947–1968. doi:10.1007/s12540-020-00705-w

Grant, K. M., Krämer, S., Löfvander, J. P., and Levi, C. G. (2007). CMAS degradation of environmental barrier coatings. *Surf. Coatings Technol.* 202 (4–7), 653–657. doi:10.1016/j.surfcoat.2007.06.045

Guipont, V., Bégué, G., Fabre, G., and Maurel, V. (2019). Buckling and interface strength analyses of thermal barrier coatings combining Laser Shock Adhesion Test to thermal cycling. *Surf. Coatings Technol.* 378, 124938. doi:10.1016/j.surfcoat.2019.124938

Gunther, B., Gradl, R., Jud, C., Eggl, E., Huang, J., Kulpe, S., et al. (2020). The versatile X-ray beamline of the Munich Compact Light Source: design, instrumentation and applications. *J. Synchrotron Radiat.* 27 (5), 1395–1414. doi:10.1107/S1600577520008309

Guo, S., Tanaka, Y., and Kagawa, Y. (2007). Effect of interface roughness and coating thickness on interfacial shear mechanical properties of EB-PVD yttria-partially stabilized zirconia thermal barrier coating systems. *J. Eur. Ceram. Soc.* 27, 3425–3431. doi:10.1016/j.jeurceramsoc.2007.02.196

Guo, S. Q., Mumm, D., Karlsson, A., and Kagawa, Y. (2005). Measurement of interfacial shear mechanical properties in thermal barrier coating systems by a barb pullout method. *Scr. Mater.* 53 (9), 1043–1048. doi:10.1016/j.scriptamat.2005.07.012

Gupta, V., Argon, A., Parks, D., and Cornie, J. (1992). Measurement of interface strength by a laser spallation technique. *J. Mech. Phys. Solids* 40 (I), 141–180. doi:10.1016/0022-5096(92)90296-E

Harder, B. J. (2020). Oxidation performance of Si-HfO2 environmental barrier coating bond coats deposited via plasma spray-physical vapor deposition. *Surf. Coatings Technol.* 384, 125311. doi:10.1016/j.surfcoat.2019.125311

Harder, B. J., Almer, J. D., Weyant, C. M., Lee, K. N., and Faber, K. T. (2009). Residual stress analysis of multilayer environmental barrier coatings. *J. Am. Ceram. Soc.* 92 (2), 452–459. doi:10.1111/J.1551-2916.2008.02888.X

Hayase, T., Waki, H., and Adachi, K. (2020). Residual stress change in thermal barrier coating due to thermal exposure evaluated by curvature method. *J. Therm. Spray Technol.* 29 (6), 1300–1312. doi:10.1007/s11666-020-01032-7

Hayashi, H., Saitou, T., Maruyama, N., Inaba, H., Kawamura, K., and Mori, M. (2005). Thermal expansion coefficient of yttria stabilized zirconia for various yttria contents. *Solid State Ionics* 176 (5–6), 613–619. doi:10.1016/j.ssi.2004.08.021

He, J., and Clarke, D. R. (1995). Determination of the piezospectroscopic coefficients for chromium-doped sapphire. *J. Am. Ceram. Soc.* 78 (5), 1347–1353. doi:10.1111/J.1151-2916.1995.TB08493.X

Hemker, K. J., and Thompson, R. J. (2007). "Thermal expansion measurements on coating materials by digital image correlation," in Proceedings of the SEM annual Conference & Exposition on Experimental & Applied Mechanics, Albuquerque, New Mexico, 1-4 June 2009.

Henderson, B., and Imbusch, G. F. (1989). *Optical spectroscopy of inorganic solids*. Oxford, United Kingdom: Oxford University Press.

Heyn, E. (1903). Short reports from the metallurgical laboratory of the royal mechanical and testing institute of charlottenburg. *Metallogr.* 5, 39–64.

Hirakata, H., Kitazawa, M., and Kitamura, T. (2005). Fatigue crack growth along interface between metal and ceramics submicron-thick films in inert environment. *Acta Mater.* 54, 89–97. doi:10.1016/j.actamat.2005.08.026

Hoffman, L. C., et al. (2023). "The effect of oxidation in environmental barrier coatings subject to foreign object damage," in ASME 2023 - Aerospace Structures, Structural Dynamics and Materials Conference, San Diego, June 19-21 2023.

Humphreys, F. J. (2001). Review Grain and subgrain characterisation by electron backscatter diffraction. *J. Mater. Sci.* 36, 3833–3854. doi:10.1023/A:1017973432592

Hutchinson, J. W., and Suo, Z. (1991). Mixed mode cracking in layered materials. *Adv. Appl. Mech.* 29, 63–191. doi:10.1016/S0065-2156(08)70164-9

Hutchinson, R. G., and Hutchinson, J. W. (2011). Lifetime assessment for thermal barrier coatings: tests for measuring mixed mode delamination toughness. *J. Am. Ceram. Soc.* 94 (1), 85–95. doi:10.1111/j.1551-2916.2011.04499.x

Iassonov, P., Gebrenegus, T., and Tuller, M. (2009). Segmentation of X-ray computed tomography images of porous materials: a crucial step for characterization and quantitative analysis of pore structures. *Water Resour. Res.* 45 (9). doi:10.1029/2009WR008087

Ilavsky, J., and Stalick, J. K. (2000). Phase composition and its changes during annealing of plasma-sprayed YSZ. *Surf. Coatings Technol.* 127, 120–129. doi:10.1016/S0257-8972(00)00562-4

Ilavsky, J., Stalick, J. K., and Wallace, J. (2001). Thermal spray yttria-stabilized zirconia phase changes during annealing. *J. Therm. Spray Technol.* 10 (3), 497–501. doi:10.1361/105996301770349277

International Digital Image Correlation Society (2018). *A good practices guide for digital image correlation*. doi:10.32720/idics/gpg.ed1

International Organization for Standardization (2015). *ISO 27307-2015: thermal spraying — evaluation of adhesion/cohesion of thermal sprayed ceramic coatings by transverse scratch testing*.

International Organization for Standardization (2020). *ISO 13067:2020 - microbeam analysis — electron backscatter diffraction — measurement of average grain size*.

International Organization for Standardization (2021). *ISO 25178-2:2021 Geometrical product specifications (GPS) — surface texture: areal — Part 2: terms, definitions and surface texture parameters*.

Irwin, G. (1948). *Fracture dynamics*. United States: American Society for Metals, 147–166.

Irwin, G. (1957). Analysis of stresses and strains near the end of a crack traversing a plate. *Trans. ASME, Ser. E, J. Appl. Mech.* 24, 361–364. doi:10.1115/1.4011547

Jacobson, N. S. (1993). Corrosion of silicon-based ceramics in combustion environments. *J. Am. Ceram. Soc.* 76 (1), 3–28. doi:10.1111/j.1151-2916.1993.tb03684.x

Jang, B. K., Nagashima, N., Kim, S., Oh, Y. S., Lee, S. M., and Kim, H. T. (2020). Mechanical properties and microstructure of Yb2SiO5 environmental barrier coatings under isothermal heat treatment. *J. Eur. Ceram. Soc.* 40 (7), 2667–2673. doi:10.1016/j.jeurceramsoc.2019.12.057

Jaya B, N., Jayaram, V., and Biswas, S. K. (2012). A new method for fracture toughness determination of graded (Pt,Ni)Al bond coats by microbeam bend tests. *Philos. Mag.* 92 (25–27), 3326–3345. doi:10.1080/14786435.2012.669068

Johnstone, A., Rickerby, D. S., and Morrell, P. (1997). "Scratch adhesion testing of TBC systems," in *High temperature surface engineering conference*.

Jones, R. L. (1997). Some aspects of the hot corrosion of thermal barrier coatings. *J. Therm. Spray Technol.* 6 (1), 77–84. doi:10.1007/BF02646315

Jones, Z. A., Sarin, P., Haggerty, R. P., and Kriven, W. M. (2013). CTEAS: a graphical-user-interface-based program to determine thermal expansion from high-temperature X-ray diffraction. *J. Appl. Cryst.* 46, 550–553. doi:10.1107/S0021889813002938

Kane, K., Garcia, E., Stack, P., Lance, M., Parker, C., Sampath, S., et al. (2021). Evaluating steam oxidation kinetics of environmental barrier coatings. *J. Am. Ceram. Soc.* 105, 590–605. doi:10.1111/jace.18093

Kane, K. A., Garcia, E., Uwanyuze, S., Lance, M., Unocic, K. A., Sampath, S., et al. (2021). Steam oxidation of ytterbium disilicate environmental barrier coatings with and without a silicon bond coat. *J. Am. Ceram. Soc.* 104 (5), 2285–2300. doi:10.1111/jace.17650

Karaoglanli, A. C., Dikici, H., and Kucuk, Y. (2013). Effects of heat treatment on adhesion strength of thermal barrier coating systems. *Eng. Fail. Anal.* 32, 16–22. doi:10.1016/j.engfailanal.2013.02.029

Kassem, R., and Al Nasiri, N. (2021). A comprehensive study on the mechanical properties of Yb2SiO5 as a potential environmental barrier coating. *Surf. Coatings Technol.* 426, 127783. doi:10.1016/J.SURFCOAT.2021.127783

Kedir, N., Garcia, E., Kirk, C., Guo, Z., Gao, J., Zhai, X., et al. (2020). *In situ* characterization of foreign object damage (FOD) in environmental-barrier-coated silicon carbide (SiC) ceramic. *J. Am. Ceram. Soc.* 103 (8), 4586–4601. doi:10.1111/jace.17165

Keller, R. R., and Geiss, R. H. (2012). Transmission EBSD from 10 nm domains in a scanning electron microscope. *J. Microsc.* 245 (3), 245–251. doi:10.1111/J.1365-2818.2011.03566.X

Kelly, T. F., and Miller, M. K. (2007). Invited review article: atom probe tomography. *Rev. Sci. Instrum.* 78 (3), 031101. doi:10.1063/1.2709758

Khoshkhou, D., Mostafavi, M., Reinhard, C., Taylor, M., Rickerby, D., Edmonds, I., et al. (2016). Three-dimensional displacement mapping of diffused Pt thermal barrier coatings via synchrotron X-ray computed tomography and digital volume correlation. *Scr. Mater.* 115, 100–103. doi:10.1016/J.SCRIPTAMAT.2015.10.033

Kim, J., Dunn, M. G., Baran, A. J., Wade, D. P., and Tremba, E. L. (1993). Deposition of volcanic materials in the hot sections of two gas turbine engines. *J. Eng. Gas Turbines Power* 115 (3), 641–651. doi:10.1115/1.2906754

Kimmel, J., Miriyala, N., Price, J., More, K., Tortorelli, P., Eaton, H., et al. (2002). Evaluation of CFCC liners with EBC after field testing in a gas turbine. *J. Eur. Ceram. Soc.* 22 (1), 2769–2775. doi:10.1016/s0955-2219(02)00142-5

Kitaoka, S., Matsudaira, T., Wada, M., Kawashima, N., Yokoe, D., and Takata, M. (2018). Mass transfer in Yb silicate environmental barrier coatings at high temperatures. *Mater. Sci. Forum* 941, 1898–1903. doi:10.4028/www.scientific.net/MSF.941.1898

Knauf, M. W., Przybyla, C. P., Ritchey, A. J., Trice, R. W., and Pipes, R. B. (2019). Residual stress determination of silicon containing boron dopants in ceramic matrix composites. *J. Am. Ceram. Soc.* 102 (5), 2820–2829. doi:10.1111/jace.15942

Knauf, M. W., Przybyla, C. P., Ritchey, A. J., Trice, R. W., and Pipes, R. B. (2020). Measuring the effects of heat treatment on SiC/SiC ceramic matrix composites using Raman spectroscopy. *J. Am. Ceram. Soc.* 103 (2), 1293–1303. doi:10.1111/jace.16724

Kobayashi, K., Kuwajima, H., and Masaki, T. (1981). Phase change and mechanical properties of ZrO2-Y2O3 solid electrolyte after ageing. *Solid State Ionics* 3 (4), 489–493. doi:10.1016/0167-2738(81)90138-7

Korsunsky, A. M. (2008). A critical discussion of the sin2ψ stress measurement technique. *Mater. Sci. Forum* 571 (572), 219–224. doi:10.4028/www.scientific.net/MSF.571-572.219

Korsunsky, A. M., Sebastiani, M., and Bemporad, E. (2009). Focused ion beam ring drilling for residual stress evaluation. *Mater. Lett.* 63, 1961–1963. doi:10.1016/j.matlet.2009.06.020

Korsunsky, A. M., Sebastiani, M., and Bemporad, E. (2010). Residual stress evaluation at the micrometer scale: analysis of thin coatings by FIB milling and digital image correlation. *Surfaces Coatings Technol.* 205, 2393–2403. doi:10.1016/j.surfcoat.2010.09.033

Krämer, S., Faulhaber, S., Chambers, M., Clarke, D., Levi, C., Hutchinson, J., et al. (2008). Mechanisms of cracking and delamination within thick thermal barrier systems in aero-engines subject to calcium-magnesium-alumino-silicate (CMAS) penetration. *Mater. Sci. Eng. A* 490, 26–35. doi:10.1016/j.msea.2008.01.006

Kulkarni, A., Goland, A., Herman, H., Allen, A. J., Dobbins, T., DeCarlo, F., et al. (2006). Advanced neutron and X-ray techniques for insights into the microstructure of EB-PVD thermal barrier coatings. *Mater. Sci. Eng. A* 426 (1–2), 43–52. doi:10.1016/j.msea.2006.03.070

Lagerlöf, K. P. D., Heuer, A. H., Castaing, J., Rivière, J. P., and Mitchell, T. E. (1994). Slip and twinning in sapphire (α-Al2O3). *J. Am. Ceram. Soc.* 77 (2), 385–397. doi:10.1111/J.1151-2916.1994.TB07006.X

Lamkin, M. A., Riley, F. L., and Fordham, R. J. (1992). Oxygen mobility in silicon dioxide and silicate glasses: a review. *J. Eur. Ceram. Soc.* 10, 347–367. doi:10.1016/0955-2219(92)90010-b

Lance, M. J., Ridley, M. J., Kane, K. A., and Pint, B. A. (2023). Raman spectroscopic characterization of SiO2 phase transformation and Si substrate stress relevant to EBC performance. *J. Am. Ceram. Soc.* 106 (10), 6205–6210. doi:10.1111/jace.19190

Lawn, B. (1993). *Fracture of brittle solids*. 2nd edn. Cambridge: Cambridge University Press.

Lee, K. N. (2000). Current status of environmental barrier coatings for Si-based ceramics. *Surf. Coatings Technol.* 133–134, 1–7. doi:10.1016/S0257-8972(00)00889-6

Lee, K. N. (2018). Yb2Si2O7 Environmental barrier coatings with reduced bond coat oxidation rates via chemical modifications for long life. *J. Am. Ceram. Soc.* 102 (3), 1507–1521. doi:10.1111/jace.15978

Lee, K. N., Garg, A., and Jennings, W. D. (2021a). Effects of the chemistry of coating and substrate on the steam oxidation kinetics of environmental barrier coatings for ceramic matrix composites. *J. Eur. Ceram. Soc.* 41, 5675–5685. doi:10.1016/j.jeurceramsoc.2021.04.037

Lee, K. N., Harder, B. J., Puleo, B. J., Almansour, A. S., Kiser, J. D., Setlock, J. A., et al. (2022). Manufacturing process development and rig validation of slurry environmental barrier coatings for SiC ceramic and SiC composite sub-components. *Coatings (Basel)* 12 (11), 1635. NA-NA. doi:10.3390/COATINGS12111635

Lee, K. N., Waters, D. L., Puleo, B. J., Garg, A., Jennings, W. D., Costa, G., et al. (2021). Development of oxide-based High temperature environmental barrier coatings for ceramic matrix composites via the slurry process. *J. Eur. Ceram. Soc.* 41, 1639–1653. doi:10.1016/j.jeurceramsoc.2020.10.012

Lee, K. N., Zhu, D., and Lima, R. S. (2021b). Perspectives on environmental barrier coatings (EBCs) manufactured via air plasma spray (APS) on ceramic matrix composites (CMCs): a tutorial paper. *J. Therm. Spray Technol.* 30, 40–58. doi:10.1007/s11666-021-01168-0

Lee, W. Y., Wright, I. G., Pint, B. A., Zhang, Y., and Liaw, P. K. (1998). Effects of sulfur impurity on the scale adhesion behavior of a desulfurized Ni-based superalloy aluminized by chemical vapor deposition. *Metallurgical Mater. Trans. A* 29A, 833–841. doi:10.1007/s11661-998-0274-z

Lesage, J., and Chicot, D. (2002). Role of residual stresses on interface toughness of thermally sprayed coatings. *Thin Solid Films* 415, 143–150. doi:10.1016/s0040-6090(02)00488-1

Levi, C. G., Hutchinson, J. W., Vidal-Sétif, M. H., and Johnson, C. A. (2012). Environmental degradation of thermal-barrier coatings by molten deposits. *MRS Bull.* 37 (10), 932–941. doi:10.1557/mrs.2012.230

Li, C., Jacques, S. D. M., Chen, Y., Daisenberger, D., Xiao, P., Markocsan, N., et al. (2016). A synchrotron X-ray diffraction deconvolution method for the measurement of residual stress in thermal barrier coatings as a function of depth. *J. Appl. Crystallogr.* 49, 1904–1911. doi:10.1107/S1600576716013935

Li, C., Xiao, P., and Cernik, R. (2019). The nondestructive measurement of strain distributions in air plasma sprayed thermal barrier coatings as a function of depth from entire Debye-Scherrer rings. *J. Appl. Crystallogr.* 53, 69–75. doi:10.1107/S1600576719016327

Li, K., Liu, J., Grovenor, C. R., and Moore, K. L. (2020). NanoSIMS imaging and analysis in materials science. *Annu. Rev. Anal. Chem.* 13, 273–292. doi:10.1146/annurev-anchem-092019-032524

Liechti, K. M., and Hanson, E. C. (1988). Nonlinear effects in mixed-mode interfacial delaminations. *Int. J. Fract.* 36, 199–217. doi:10.1007/BF00035100

Lima, C. R. C., Dosta, S., Guilemany, J., and Clarke, D. (2017). The application of photoluminescence piezospectroscopy for residual stresses measurement in thermally sprayed TBCs. *Surf. Coatings Technol.* 318, 147–156. doi:10.1016/J.SURFCOAT.2016.07.084

Lima, R. S. (2020). Perspectives on thermal gradients in porous ZrO2-7–8 wt.% Y2O3 (YSZ) thermal barrier coatings (TBCs) manufactured by air plasma spray (APS). *Plasma Spray. (APS), Coatings* 10 (9), 812. doi:10.3390/coatings10090812

Lopez, E., Beltzung, F., and Zambelli, G. (1989). Measurement of cohesion and adhesion strengths in alumina coatings produced by plasma spraying. *J. Mater. Sci. Lett.* 8, 346–348. doi:10.1007/BF00725519

Lu, J., Chen, Y., Zhang, H., Zhao, C., Zhao, X., Guo, F., et al. (2019). Superior oxidation and spallation resistant NiCoCrAlY bond coat via homogenizing the yttrium distribution. *Corros. Sci.* 159, 108145. doi:10.1016/J.CORSCI.2019.108145

Luo, Q., and Jones, A. H. (2010). High-precision determination of residual stress of polycrystalline coatings using optimised XRD-sin2ψ technique. *Surf. Coatings Technol.* 205 (5), 1403–1408. doi:10.1016/J.SURFCOAT.2010.07.108

Mahfouz, L., Marchand, B., Guipont, V., Coudon, F., and Maurel, V. (2023). Driving forces in thermal barrier coatings blistering. *Materialia* 28, 101728. doi:10.1016/j.mtla.2023.101728

Maire, E., and Withers, P. J. (2014). Quantitative X-ray tomography. *Int. Mater. Rev.* 59 (1), 1–43. doi:10.1179/1743280413Y.0000000023

Mao, W. G., Wan, J., Dai, C., Ding, J., Zhang, Y., Zhou, Y., et al. (2012). Evaluation of microhardness, fracture toughness and residual stress in a thermal barrier coating system: a modified Vickers indentation technique. *Surfaces Coatings Technol.* 206, 4455–4461. doi:10.1016/j.surfcoat.2012.02.060

Marquis, E. A., Bachhav, M., Chen, Y., Dong, Y., Gordon, L. M., and McFarland, A. (2013). On the current role of atom probe tomography in materials characterization and materials science. *Curr. Opin. Solid State Mater. Sci.* 17, 217–223. doi:10.1016/j.cossms.2013.09.003

Martins, J. P., Chen, Y., Brewster, G., McIntyre, R., and Xiao, P. (2020). Investigation of the bond coat interface topography effect on lifetime, microstructure and mechanical properties of air-plasma sprayed thermal barrier coatings. *J. Eur. Ceram. Soc.* 40 (15), 5719–5730. doi:10.1016/J.JEURCERAMSOC.2020.05.082

Martins, J. P., Yu, H., Chen, Y., Brewster, G., McIntyre, R., and Xiao, P. (2021). Effect of bond coat topography on the fracture mechanics and lifetime of air-plasma sprayed thermal barrier coatings. *Surf. Coatings Technol.* 421, 127447. doi:10.1016/j.surfcoat.2021.127447

Matsudaira, T., Wada, M., Kawashima, N., Takeuchi, M., Yokoe, D., Kato, T., et al. (2021). Mass transfer in polycrystalline ytterbium monosilicate under oxygen potential gradients at high temperatures. *J. Eur. Ceram. Soc.* 41, 3150–3160. doi:10.1016/j.jeurceramsoc.2020.07.045

Mauer, G., and Vaßen, R. (2020). Coatings with columnar microstructures for thermal barrier applications. *Adv. Eng. Mater.* 22 (6). doi:10.1002/adem.201900988

Maurel, V., Guipont, V., Theveneau, M., Marchand, B., and Coudon, F. (2019). Thermal cycling damage monitoring of thermal barrier coating assisted with LASAT (LAser Shock Adhesion Test). *Surf. Coatings Technol.* 380, 125048. doi:10.1016/j.surfcoat.2019.125048

Mccormack, S., Cao, H., Martins, J. P., Withers, P. J., and Xiao, P. (2023). The effect of porosity, mixed molecular/Knudsen diffusion, and a surface barrier layer on steam corrosion of Yb2Si2O7. *Corros. Sci.* 219, 111238. doi:10.1016/j.corsci.2023.111238

Mccusker, L. B., Von Dreele, R. B., Cox, D. E., Louër, D., and Scardi, P. (1999). Rietveld refinement guidelines. *J. Appl. Crystallogr.* 32, 36–50. doi:10.1107/S0021889898009856

Medricky, J., Curry, N., Pala, Z., Vilemova, M., Chraska, T., Johansson, J., et al. (2015). Optimization of high porosity thermal barrier coatings generated with a porosity former. *J. Therm. Spray Technol.* 24 (4), 622–628. doi:10.1007/s11666-014-0214-y

Medvedovski, E. (2001). Wear-resistant engineering ceramics. *Wear* 249, 821–828. doi:10.1016/S0043-1648(01)00820-1

Mercer, C., Faulhaber, S., Evans, A., and Darolia, R. (2005). A delamination mechanism for thermal barrier coatings subject to calcium-magnesium-alumino-silicate (CMAS) infiltration. *Acta Mater.* 53, 1029–1039. doi:10.1016/j.actamat.2004.11.028

Miller, M. K., and Kenik, E. A. (2004). Atom probe tomography: a technique for nanoscale characterization. *Microsc. Microanal.* 10, 336–341. doi:10.1017/S1431927604040577

Miller, M. K., Russell, K. F., Thompson, K., Alvis, R., and Larson, D. J. (2007). Review of atom probe FIB-based specimen preparation methods. *Microsc. Microanal.* 13, 428–436. doi:10.1017/S1431927607070845

Miller, R. A. (1987). Current status of thermal barrier coatings - an overview. *Surf. Coatings Technol.* 30, 1–11. doi:10.1016/0257-8972(87)90003-X

Miller, R. A. (1997). Thermal barrier coatings for aircraft engines: history and directions. *J. Therm. Spray Technol.* 6 (1), 35–42. doi:10.1007/BF02646310

Mitchell, T. E., and Heuer, A. H. (2005). "Dislocations and mechanical properties of ceramics," in *Dislocations in solids* (Amsterdam, Netherlands: Elsevier), 339–402.

Morelli, S., Bursich, S., Testa, V., Bolelli, G., Miccichè, A., and Lusvarghi, L. (2022). CMAS corrosion and thermal cycling fatigue resistance of alternative thermal barrier coating materials and architectures: a comparative evaluation. *Surf. Coatings Technol.* 439 (January), 128433. doi:10.1016/j.surfcoat.2022.128433

Morrell, P., and Rickerby, D. S. (1998). *Advantages/disadvantages of various TBC systems as perceived by the engine manufacturer*.

Motz, C., Schöberl, T., and Pippan, R. (2005). Mechanical properties of micro-sized copper bending beams machined by the focused ion beam technique. *Acta Mater.* 53 (15), 4269–4279. doi:10.1016/J.ACTAMAT.2005.05.036

Nagelberg, A. S. (1985). Destabilization of yttria-stabilized zirconia induced by molten sodium vanadate-sodium sulfate melts. *J. Electrochem. Soc.* 132 (10), 2502–2507. doi:10.1149/1.2113609

Nakamura, T., Qian, G., and Berndt, C. C. (2000). Effects of pores on mechanical properties of plasma-sprayed ceramic coatings. *J. Am. Ceram. Soc.* 83 (3), 578–584. doi:10.1111/j.1151-2916.2000.tb01236.x

Nakano, N., Marville, L., and Reif, R. (1992). Raman scattering in polycrystalline silicon doped with boron. *J. Appl. Phys.* 72, 3641–3647. doi:10.1063/1.352307

Naraparaju, R., Hüttermann, M., Schulz, U., and Mechnich, P. (2017). Tailoring the EB-PVD columnar microstructure to mitigate the infiltration of CMAS in 7YSZ thermal barrier coatings. *J. Eur. Ceram. Soc.* 37, 261–270. doi:10.1016/j.jeurceramsoc.2016.07.027

Noebe, R. D., Bowman, R. R., and Nathal, M. V. (1993). Physical and mechanical properties of the B2 compound NiAl. *Int. Mater. Rev.* 38 (4), 193–232. doi:10.1179/imr.1993.38.4.193

Nohava, J., Bonferroni, B., Bolelli, G., and Lusvarghi, L. (2010). Interesting aspects of indentation and scratch methods for characterization of thermally-sprayed coatings. *Surf. Coatings Technol.* 205 (4), 1127–1131. doi:10.1016/j.surfcoat.2010.08.086

Ntziouni, A., Thomson, J., Xiarchos, I., Li, X., Bañares, M. A., Charitidis, C., et al. (2022). Review of existing standards, guides, and practices for Raman spectroscopy. *Appl. Spectrosc.* 76 (7), 747–772. doi:10.1177/00037028221090988

Nychka, J. A., and Clarke, D. R. (2001). Damage quantification in TBCs by photo-stimulated luminescence spectroscopy. *Surf. Coatings Technol.* 146–147, 110–116. doi:10.1016/S0257-8972(01)01455-4

Nye, J. F. (1957). *Physical properties of crystals*. Oxford: Oxford University Press.

Ochiai, Y., Nannichi, Y., and Masuda, K. (1980). Quantitative analysis of the wide range of concentrations of boron in silicon by SIMS. *Jpn. J. Appl. Phys.* 19 (12), L777–L779. doi:10.1143/JJAP.19.L777

Ochrombel, R., Schneider, J., Hildmann, B., and Saruhan, B. (2010). Thermal expansion of EB-PVD yttria stabilized zirconia. *J. Eur. Ceram. Soc.* 30 (12), 2491–2496. doi:10.1016/J.JEURCERAMSOC.2010.05.008

Oliver, W. C., and Pharr, G. M. (2004). Measurement of hardness and elastic modulus by instrumented indentation: advances in understanding and refinements to methodology. *J. Mater. Res.* 19, 3–20. doi:10.1557/jmr.2004.19.1.3

Opila, E. J., and Smialek, J. L. (1999). SiC recession caused by SiO2 scale volatility under combustion conditions: I. Experimental results and empirical model. *J. Am. Ceram. Soc.* 82 (7), 1817–1825. doi:10.1111/j.1151-2916.1999.tb02004.x

Padture, N. P. (2019). Environmental degradation of high-temperature protective coatings for ceramic-matrix composites in gas-turbine engines. *npj Mater. Degrad.* 3 (1), 11–16. doi:10.1038/s41529-019-0075-4

Paksoy, A. H., Martins, J. P., Cao, H., Chen, Y., Gibson, G., and Xiao, P. (2022). Influence of alumina addition on steam corrosion behaviour of ytterbium disilicates for environmental barrier coating applications. *Corros. Sci.* 207, 110555. doi:10.1016/j.corsci.2022.110555

Paksoy, A. H., and Xiao, P. (2021). Study on sintering behaviour of ytterbium disilicate and ytterbium monosilicate for environmental barrier coating applications. *Ceram. Int.* 48 (8), 11238–11250. doi:10.1016/j.ceramint.2021.12.344

Paksoy, A. H., and Xiao, P. (2023). Review of processing and design methodologies of environmental barrier coatings for next generation gas turbine applications. *Adv. Appl. Ceram. Prepr.* 122, 36–56. doi:10.1080/17436753.2023.2193783

Peacor, D. R. (1973). High-temperature single-crystal study of the cristobalite inversion. *Z. fur Kristallogr.* 138, 274–298. doi:10.1524/zkri.1973.138.138.274

Perrotta, A. J., Grubbs, D. K., Martin, E. S., Dando, N. R., McKinstry, H. A., and Huarg, C. (1989). Chemical stabilization of β-cristobalite. *J. Am. Ceram. Soc.* 72 (3), 441–447. doi:10.1111/j.1151-2916.1989.tb06150.x

Piva, A., and Viola, E. (1980). Biaxial load effects on a crack between dissimilar media. *Eng. Fract. Mech.* 13, 143–174. doi:10.1016/0013-7944(80)90049-1

Poerschke, D. L., Jackson, R. W., and Levi, C. G. (2017). Silicate deposit degradation of engineered coatings in gas turbines: progress toward models

and materials solutions. *Annu. Rev. Mater. Res.* 47, 297–330. doi:10.1146/annurev-matsci-010917-105000

Presby, M. J., Stokes, J. L., and Harder, B. J. (2023). Solid particle erosion in ceramic matrix composites and environmental barrier coatings: a perspective. *J. Am. Ceram. Soc.*, 1–17. doi:10.1111/jace.19376

Reed, R. C. (2006). "Environmental degradation: the role of coatings," in *The superalloys: fundamentals and applications*, 283–350. doi:10.1017/CBO9780511541285.007

Richards, B. T., Begley, M. R., and Wadley, H. N. G. (2015a). Mechanisms of ytterbium monosilicate/mullite/silicon coating failure during thermal cycling in water vapor. *J. Am. Ceram. Soc.* 98 (12), 4066–4075. doi:10.1111/jace.13792

Richards, B. T., Young, K. A., de Francqueville, F., Sehr, S., Begley, M. R., and Wadley, H. N. (2016). Response of ytterbium disilicate-silicon environmental barrier coatings to thermal cycling in water vapor. *Acta Mater.* 106, 1–14. doi:10.1016/j.actamat.2015.12.053

Richards, B. T., Zhao, H., and Wadley, H. N. G. (2015b). Structure, composition, and defect control during plasma spray deposition of ytterbium silicate coatings. *J. Mater. Sci.* 50 (24), 7939–7957. doi:10.1007/s10853-015-9358-5

Richards, B. T., Zhu, D., and Hardley, H. N. G. (2015). "Mechanical properties of air plasma sprayed environmental barrier coating (EBC) systems: preliminary assessments," in 39th International Conference on Advanced Ceramics and Composites, Daytona Beach, Florida, 2015 January 25-30, 219–237. doi:10.1002/9781119211747.ch18

Ridley, M., Garcia, E., Kane, K., Sampath, S., and Pint, B. (2023). Environmental barrier coatings on enhanced roughness SiC: effect of plasma spraying conditions on properties and performance. *J. Eur. Ceram. Soc.* 43, 6473–6481. doi:10.1016/j.jeurceramsoc.2023.06.049

Ridley, M., Kane, K., Lance, M., Parker, C., Su, Y., Sampath, S., et al. (2022). Steam oxidation and microstructural evolution of rare earth silicate environmental barrier coatings. *J. Am. Ceram. Soc.* 106, 613–620. doi:10.1111/jace.18769

Rodríguez-Viejo, J., Sibieude, F., Clavaguera-Mora, M. T., and Monty, C. (1993). 18O diffusion through amorphous SiO2 and cristobalite. *Appl. Phys. Lett.* 63 (14), 1906–1908. doi:10.1063/1.110644

Roebuck, B. (2008). *Measurement good practice guide No. 9: palmqvist toughness for hard and brittle materials.*

Rohbeck, N., Morrell, P., and Xiao, P. (2019). Degradation of ytterbium disilicate environmental barrier coatings in high temperature steam atmosphere. *J. Eur. Ceram. Soc.* 39, 3153–3163. doi:10.1016/j.jeurceramsoc.2019.04.034

Rouquerol, J., Baron, G., Denoyel, R., Giesche, H., Groen, J., Klobes, P., et al. (2012). Liquid intrusion and alternative methods for the characterization of macroporous materials (IUPAC Technical Report). *Pure Appl. Chem.* 84 (1), 107–136. doi:10.1351/PAC-REP-10-11-19

Salanova, A., Brummel, I. A., Yakovenko, A. A., Opila, E. J., and Ihlefeld, J. F. (2023). Phase stability and tensorial thermal expansion properties of single to high-entropy rare-earth disilicates. *J. Am. Ceram. Soc.* 106, 3228–3238. doi:10.1111/jace.18986

Saruhan, B., Ryukhtin, V., and Kelm, K. (2011). Correlation of thermal conductivity changes with anisotropic nano-pores of EB-PVD deposited FYSZ-coatings. *Surf. Coatings Technol.* 205 (23–24), 5369–5378. doi:10.1016/J.SURFCOAT.2011.05.051

Schindelin, J., Arganda-Carreras, I., Frise, E., Kaynig, V., Longair, M., Pietzsch, T., et al. (2012). Fiji: an open-source platform for biological-image analysis. *Nat. Methods* 9 (7), 676–682. doi:10.1038/nmeth.2019

Schlichting, K. W., Vaidyanathan, K., Sohn, Y., Jordan, E., Gell, M., and Padture, N. (2000). Application of Cr 3+ photoluminescence piezo-spectroscopy to plasma-sprayed thermal barrier coatings for residual stress measurement. *Mater. Sci. Eng. A* 291, 68–77. doi:10.1016/S0921-5093(00)00973-4

Scott, H. G. (1975). Phase relationships in the zirconia-yttria system. *J. Mater. Sci.* 10, 1527–1535. doi:10.1007/bf01031853

Selcuk, A., and Atkinson, A. (2002). Analysis of the Cr3+ luminescence spectra from thermally grown oxide in thermal barrier coatings. *Mater. Sci. Eng. A* 335 (1–2), 147–156. doi:10.1016/S0921-5093(01)01911-6

Selçuk, A., and Atkinson, A. (2003). The evolution of residual stress in the thermally grown oxide on Pt diffusion bond coats in TBCs. *Acta Mater.* 51 (2), 535–549. doi:10.1016/S1359-6454(02)00436-6

Sheppard, A. P., Sok, R. M., and Averdunk, H. (2004). Techniques for image enhancement and segmentation of tomographic images of porous materials. *Phys. A Stat. Mech. Its Appl.* 339 (1–2), 145–151. doi:10.1016/J.PHYSA.2004.03.057

Shillington, E. A. G., and Clarke, D. R. (1999). Spalling failure of a thermal barrier coating associated with aluminum depletion in the bond-coat. *Acta Mater.* 47 (4), 1297–1305. doi:10.1016/s1359-6454(98)00407-8

Siddiqui, S. F., Knipe, K., Manero, A., Meid, C., Wischek, J., Okasinski, J., et al. (2013). Synchrotron X-ray measurement techniques for thermal barrier coated cylindrical samples under thermal gradients. *Rev. Sci. Instrum.* 84, 083904. doi:10.1063/1.4817543

Siebert, B., Funke, C., Vaβen, R., and Stöver, D. (1999). Changes in porosity and Youngs Modulus due to sintering of plasma sprayed thermal barrier coatings. *J. Mater. Process. Technol.* 92 (93), 217–223. doi:10.1016/S0924-0136(99)00243-5

Singh, J., and Wolfe, D. E. (2005). Review Nano and macro-structured component fabrication by electron beam-physical vapor deposition (EB-PVD). *J. Mater. Sci.* 40, 1–26. doi:10.1007/s10853-005-5682-5

Smith, A. D. (2022). "Automated *in-situ* mechanical testing of heavily textured Ti6Al4V to obtain high spatial and temporal resolution strain maps," in 16th Multinational Congress on Microscopy (MCM16), Brno, September 4th-9th 2022. doi:10.1016/j.actamat.2022.117691

Song, N., Wang, Z., Xing, Y., Zhang, M., Wu, P., Qian, F., et al. (2019). Evaluation of phase transformation and mechanical properties of metastable yttria-stabilized zirconia by nanoindentation. *Materials* 12 (10), 1677. doi:10.3390/MA12101677

Spitsberg, I., and Steibel, J. (2004). Thermal and environmental barrier coatings for SiC/SiC CMCs in aircraft engine applications. *Int. J. Appl. Ceram. Technol.* 1 (4), 291–301. doi:10.1111/J.1744-7402.2004.TB00181.X

Stack, P. (2022). Size of oxidation feature from image analysis. Available at: https://github.com/TriplePointCat/SOFIA-CV.

Stecura, S. (1978). "Effects of compositional changes on the performance of a thermal barrier coating system," in *Annual conference on composite and advanced materials*.

Stecura, S. (1985). Optimization of the NiCrAl-Y/ZrO2-Y2O3 thermal barrier system. *NASA Tech. Memo.*

Sternlicht, H., McComb, D. W., and Padture, N. P. (2022a). Interaction of ytterbium pyrosilicate environmental-barrier-coating ceramics with molten calcia-magnesia-aluminosilicate glass: Part I, Microstructures. *Acta Mater.* 241, 118360. doi:10.1016/J.ACTAMAT.2022.118360

Sternlicht, H., McComb, D. W., and Padture, N. P. (2022b). Interaction of ytterbium pyrosilicate environmental-barrier-coating ceramics with molten calcia-magnesia-aluminosilicate glass: Part II, Interfaces. *Acta Mater.* 241, 118359. doi:10.1016/J.ACTAMAT.2022.118359

Stiger, M. J., Yanar, M. M., Topping, M. G., Pettit, F. S., and Meier, G. H. (1999). Thermal barrier coatings for the 21st century. *Z. fur Met.* 90 (12), 1069–1078. doi:10.1515/ijmr-1999-901218

Stolzenburg, F., Almer, J., Lee, K. N., Harder, B. J., and Faber, K. T. (2011). "Stresses in ytterbium silicate multilayer environmental barrier coatings," in Denver X-ray Conference, Colorado, August 1–5, 2011, 106–115.

Stolzenburg, F., Kenesei, P., Almer, J., Lee, K., Johnson, M., and Faber, K. (2016a). The influence of calcium-magnesium-aluminosilicate deposits on internal stresses in Yb2Si2O7 multilayer environmental barrier coatings. *Acta Mater.* 105, 189–198. doi:10.1016/j.actamat.2015.12.016

Stolzenburg, F., Kenesei, P., Almer, J., Lee, K., Johnson, M., and Faber, K. (2016b). The influence of calcium–magnesium–aluminosilicate deposits on internal stresses in Yb2Si2O7 multilayer environmental barrier coatings. *Acta Mater.* 105, 189–198. doi:10.1016/J.ACTAMAT.2015.12.016

Stoney, G. G. (1909). The tension of metallic films deposited by electrolysis. *Proc. R. Soc. A* 82 (553), 172–175. doi:10.1098/rspa.1909.0021

Stott, F. H., De Wet, D. J., and Taylor, R. (1994). Degradation of thermal-barrier coatings at very high temperatures. *MRS Bull.* 19 (10), 46–49. doi:10.1557/s0883769400048223

Stott, F. H., and Wood, G. C. (1987). Growth and adhesion of oxide scales on Al2O3 forming alloys and coatings. *Mater. Sci. Eng.* 8, 267–274. doi:10.1016/0025-5416(87)90388-0

Stuckner, J., Harder, B., and Smith, T. M. (2022). Microstructure segmentation with deep learning encoders pre-trained on a large microscopy dataset. *npj Comput. Mater.* 8 (1), 200. doi:10.1038/s41524-022-00878-5

Su, Y. F., Stack, P. I. M., Stephens, C. J., Kane, K. A., Pillai, R., Pint, B. A., et al. (2021). *Quantifying high temperature corrosion*. United States: NACE Corrosion 2021, C2021–C16805.

Suo, Z., and Hutchinson, J. W. (1990). Interface crack between two elastic layers. *Int. J. Fract.* 43, 1–18. doi:10.1007/BF00018123

Swainson, I. P., Dove, M. T., and Palmer, D. C. (2003). Infrared and Raman spectroscopy studies of the α-β phase transition in cristobalite. *Phys. Chem. Minerals* 30 (6), 353–365. doi:10.1007/s00269-003-0320-8

Takahashi, R. J., Assis, J. M. K., Piorino Neto, F., and Reis, D. A. P. (2019). Heat treatment for TGO growth on NiCrAlY for TBC application. *Mater. Res. Express* 6, 126442. doi:10.1088/2053-1591/ab6778

Tanaka, M., Hasegaw, M., Dericioglu, A. F., and Kagawa, Y. (2006). Measurement of residual stress in air plasma-sprayed Y2O3-ZrO2 thermal barrier coating system using micro-Raman spectroscopy. *Mater. Sci. Eng. A* 419. doi:10.1016/j.msea.2005.12.034

Tanaka, M., Kitazawa, R., Tomimatsu, T., Liu, Y., and Kagawa, Y. (2009). Residual stress measurement of an EB-PVD Y2O3-ZrO2 thermal barrier coating by micro-Raman spectroscopy. *Surf. Coatings Technol.* 204 (5), 657–660. doi:10.1016/J.SURFCOAT.2009.08.042

Tejero-Martin, D., Bai, M., Mata, J., and Hussain, T. (2021). Evolution of porosity in suspension thermal sprayed YSZ thermal barrier coatings through neutron scattering and image analysis techniques. *J. Eur. Ceram. Soc.* 41 (12), 6035–6048. doi:10.1016/j.jeurceramsoc.2021.04.020

Tejero-Martin, D., Bennett, C., and Hussain, T. (2021). A review on environmental barrier coatings: history, current state of the art and future developments. *J. Eur. Ceram. Soc.* 41 (3), 1747–1768. doi:10.1016/J.JEURCERAMSOC.2020.10.057

Tejero-Martin, D., Romero, A. R., Wellman, R. G., and Hussain, T. (2022). Interaction of CMAS on thermal sprayed ytterbium disilicate environmental barrier coatings: a story of porosity. *Ceram. Int.* 48, 8286–8296. doi:10.1016/j.ceramint.2021.12.033

The British Standards Institution (2016). *BS ISO 15901-1:2016 Evaluation of pore size distribution and porosity of solid materials by mercury porosimetry and gas adsorption*.

Toby, B. H., and Von Dreele, R. B. (2013). GSAS-II: the genesis of a modern open-source all purpose crystallography software package. *J. Appl. Crystallogr.* 46 (2), 544–549. doi:10.1107/S0021889813003531

Tolpygo, V. K., and Clarke, D. R. (1998). Wrinkling of α-alumina films grown by thermal oxidation—I. Quantitative studies on single crystals of Fe–Cr–Al alloy. *Acta Mater.* 46 (14), 5153–5166. doi:10.1016/S1359-6454(98)00133-5

Tolpygo, V. K., and Clarke, D. R. (2000). Surface rumpling of a (Ni, Pt)Al bond coat induced by cyclic oxidation. *Acta Mater.* 48, 3283–3293. doi:10.1016/S1359-6454(00)00156-7

Trimby, P. W. (2012). Orientation mapping of nanostructured materials using transmission Kikuchi diffraction in the scanning electron microscope. *Ultramicroscopy* 120, 16–24. doi:10.1016/j.ultramic.2012.06.004

Vasinonta, A., and Beuth, J. L. (2001). Measurement of interfacial toughness in thermal barrier coating systems by indentation. *Eng. Fract. Mech.* 68, 843–860. doi:10.1016/S0013-7944(00)00130-2

Vencl, A., Arostegui, S., Favaro, G., Zivic, F., Mrdak, M., Mitrović, S., et al. (2011). Evaluation of adhesion/cohesion bond strength of the thick plasma spray coatings by scratch testing on coatings cross-sections. *Tribol. Int.* 44 (11), 1281–1288. doi:10.1016/J.TRIBOINT.2011.04.002

Vidakis, N., Antoniadis, A., and Bilalis, N. (2003). The VDI 3198 indentation test evaluation of a reliable qualitative control for layered compounds. *J. Mater. Process. Technol.* 143-144, 481–485. doi:10.1016/S0924-0136(03)00300-5

Wada, K., Yamaguchi, N., and Matsubara, H. (2004). Crystallographic texture evolution in ZrO2–Y2O3 layers produced by electron beam physical vapor deposition. *Surf. Coatings Technol.* 184 (1), 55–62. doi:10.1016/J.SURFCOAT.2003.08.084

Wada, M., Matsudaira, T., Kawashima, N., Kitaoka, S., and Takata, M. (2017). Mass transfer in polycrystalline ytterbium disilicate under oxygen potential gradients at high temperatures. *Acta Mater.* 135, 372–381. doi:10.1016/j.actamat.2017.06.029

Wang, X., and Atkinson, A. (2007). Piezo-spectroscopic mapping of the thermally grown oxide in thermal barrier coatings. *Mater. Sci. Eng. A* 465, 49–58. doi:10.1016/j.msea.2007.04.081

Wang, X., Wang, C., and Atkinson, A. (2012). Interface fracture toughness in thermal barrier coatings by cross-sectional indentation. *Acta Mater.* 60, 6152–6163. doi:10.1016/j.actamat.2012.07.058

Wěiss, Z., and Marshall, K. (1997). Elemental depth profiling of coated and surface-modified materials by GD-OES: hard coatings on cutting tools. *Thin Solid Films* 308 (309), 382–388. doi:10.1016/S0040-6090(97)00586-5

Wellman, R. G., and Nicholls, J. R. (2004). On the effect of ageing on the erosion of EB-PVD TBCs. *Surf. Coatings Technol.* 177–178, 80–88. doi:10.1016/j.surfcoat.2003.06.019

Wellman, R. G., and Nicholls, J. R. (2007). A review of the erosion of thermal barrier coatings. *J. Phys. D Appl. Phys.* 40 (16), 293–305. doi:10.1088/0022-3727/40/16/R01

Wellman, R. G., and Nicholls, J. R. (2008). Erosion, corrosion and erosion-corrosion of EB PVD thermal barrier coatings. *Tribol. Int.* 41 (7), 657–662. doi:10.1016/j.triboint.2007.10.004

Whitehouse, D. J. (1997). Surface metrology. *Meas. Sci. Technol.* 8, 955–972. doi:10.1088/0957-0233/8/9/002

Winchester, M. R., and Payling, R. (2004). Radio-frequency glow discharge spectrometry:. *Spectrochim. Acta - Part B At. Spectrosc.* 59 (5), 607–666. doi:10.1016/j.sab.2004.02.013

Withers, P. J., and Bhadeshia, H. K. D. H. (2001). Residual stress part 1 - measurement techniques. *Mater. Sci. Technol.* 17 (4), 355–365. doi:10.1179/026708301101509980

Witz, G., Shklover, V., Steurer, W., Bachegowda, S., and Bossmann, H. (2007). Phase evolution in yttria-stabilized zirconia thermal barrier coatings studied by rietveld refinement of X-ray powder diffraction patterns. *J. Am. Ceram. Soc.* 90 (9), 2935–2940. doi:10.1111/J.1551-2916.2007.01785.X

Xiao, J., Guo, Q., Wei, L., He, W., and Guo, H. (2020). Microstructures and phases of ytterbium silicate coatings prepared by plasma spray-physical vapor deposition. *Materials* 13 (7), 1721. doi:10.3390/ma13071721

Yanar, N. M., Pettit, F. S., and Meier, G. H. (2006). Failure characteristics during cyclic oxidation of Yttria stabilized zirconia thermal barrier coatings deposited via electron beam physical vapor deposition on platinum aluminide and on NiCoCrAlY bond coats with processing modifications for improved performances. *Metallurgical Mater. Trans. A Phys. Metallurgy Mater. Sci.* 37 (5), 1563–1580. doi:10.1007/s11661-006-0100-4

Yilmaz, E., Paksoy, A. H., Gibson, G., and Xiao, P. (2023). Constrained sintering and thermal ageing behaviour of electrophoretically deposited Yb2Si2O7 environmental barrier coating. *J. Eur. Ceram. Soc.* 43 (14), 6427–6439. doi:10.1016/j.jeurceramsoc.2023.06.025

Yilmaz, E., and Xiao, P. (2022). Effects of suspension properties on the fabrication of Yb2Si2O7 coatings using electrophoretic deposition. *J. Eur. Ceram. Soc.* 42 (2), 638–648. doi:10.1016/j.jeurceramsoc.2021.10.038

Yu, H., and Clarke, D. R. (2002). Effect of codoping on the R-line luminescence of Cr3+-doped alumina. *J. Am. Ceram. Soc.* 85 (8), 1966–1970. doi:10.1111/j.1151-2916.2002.tb00389.x

Yuan, M., Liu, L., Wang, J., Hu, Q., Zhang, H., Zhang, S., et al. (2022). Crack-healing behaviour of MoSi2 dispersed Yb2Si2O7 environmental barrier coatings. *Ceram. Int.* 48 (20), 29919–29928. doi:10.1016/j.ceramint.2022.06.258

Zhang, X., Kulczyk-Malecka, J., Carr, J., Xiao, P., and Withers, P. (2018). 3D characterization of porosity in an air plasma-sprayed thermal barrier coating and its effect on thermal conductivity. *J. Am. Ceram. Soc.* 101 (6), 2482–2492. doi:10.1111/jace.15409

Zhang, X., Li, C., Withers, P. J., Markocsan, N., and Xiao, P. (2019). Determination of local residual stress in an air plasma spray thermal barrier coating (APS-TBC) by microscale ring coring using a picosecond laser. *Scr. Mater.* 167, 126–130. doi:10.1016/j.scriptamat.2019.03.036

Zhang, X., Shan, X., Withers, P. J., Zhao, X., and Xiao, P. (2020). Tracking the calcium-magnesium-alumino-silicate (CMAS) infiltration into an air-plasma spray thermal barrier coating using X-ray imaging. *Scr. Mater.* 176 94–98. doi:10.1016/J.SCRIPTAMAT.2019.09.016

Zhang, Z., Park, Y., Xue, Z., Zhang, S., Byon, E., and Koo, B. (2022). Research status of bond coats in environmental barrier coatings. *Int. J. Appl. Ceram. Technol.* 19 (4), 1841–1859. doi:10.1111/IJAC.14042

Zhao, C., Zhou, Y., Zou, Z., Luo, L., Zhao, X., Guo, F., et al. (2017). Effect of alloyed Lu, Hf and Cr on the oxidation and spallation behavior of NiAl. *Corros. Sci.* 126, 334–343. doi:10.1016/j.corsci.2017.07.016

Zhao, G., Xu, B., Ren, K., Shao, G., and Wang, Y. (2020). Oxygen diffusion through environmental barrier coating materials. *Ceram. Int.* 46, 19545–19549. doi:10.1016/j.ceramint.2020.05.007

Zhao, P. F., Sun, C., Zhu, X., Shang, F., and Li, C. (2010). Fracture toughness measurements of plasma-sprayed thermal barrier coatings using a modified four-point bending method. *Surf. Coatings Technol.* 204 (24), 4066–4074. doi:10.1016/J.SURFCOAT.2010.05.029

Zhao, X., Liu, J., Rickerby, D., Jones, R., and Xiao, P. (2011). Evolution of interfacial toughness of a thermal barrier system with a Pt-diffused γ/γ′bond coat. *Acta Mater.* 59, 6401–6411. doi:10.1016/j.actamat.2011.07.001

Zhao, X., Shapiro, I. P., and Xiao, P. (2008). Spinel formation in thermal barrier systems with a Pt-enriched γ-Ni + γ′-Ni3Al bond coat. *Surf. Coatings Technol.* 202 (13), 2905–2916. doi:10.1016/J.SURFCOAT.2007.10.030

Zhao, X., and Xiao, P. (2006). Residual stresses in thermal barrier coatings measured by photoluminescence piezospectroscopy and indentation technique. *Surf. Coatings Technol.* 201, 1124–1131. doi:10.1016/j.surfcoat.2006.01.035

Zhao, Y., Shinmi, A., Zhao, X., Withers, P., Van Boxel, S., Markocsan, N., et al. (2012). Investigation of interfacial properties of atmospheric plasma sprayed thermal barrier coatings with four-point bending and computed tomography technique. *Surf. Coatings Technol.* 206, 4922–4929. doi:10.1016/j.surfcoat.2012.05.099

Zhong, X., Niu, Y., Li, H., Zhou, H., Dong, S., Zheng, X., et al. (2018). Thermal shock resistance of tri-layer Yb2SiO5/Yb2Si2O7/Si coating for SiC and SiC-matrix composites. *J. Am. Ceram. Soc.* 101 (10), 4743–4752. doi:10.1111/jace.15713

Zhou, D., Guillon, O., and Vaßen, R. (2017). Development of YSZ thermal barrier coatings using axial suspension plasma spraying. *Coatings* 7, 120. doi:10.3390/COATINGS7080120

Zhu, D., and Miller, R. (2000). Thermal conductivity and elastic modulus evolution of thermal barrier coatings under high heat flux conditions. *J. Therm. Spray Technol.* 9, 175–180. doi:10.1361/105996300770349890

Zhu, J. G., Xie, H. M., Li, Y. J., Luo, Q., and Gu, C. Z. (2014). Interfacial residual stress analysis of thermal spray coatings by miniature ring-core cutting combined with DIC method. *Exp. Mech.* 54, 127–136. doi:10.1007/s11340-012-9640-2

Zhu, W., Cai, X., Yang, L., Xia, J., Zhou, Y., and Pi, Z. (2018). The evolution of pores in thermal barrier coatings under volcanic ash corrosion using X-ray computed tomography. *Surf. Coatings Technol.* 357, 372–378. doi:10.1016/j.surfcoat.2018.10.029